



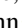






Systematic evidence for quasifission in ${}^9\text{Be}$ -, ${}^{12}\text{C}$ -, and ${}^{16}\text{O}$ -induced reactions forming ${}^{258,260}\text{No}$

T. Banerjee ^{1,*}, D. J. Hinde¹, D. Y. Jeung ¹, K. Banerjee ^{1,2}, M. Dasgupta¹, A. C. Berriman¹, L. T. Bezzina ¹, H. M. Albers³, Ch. E. Düllmann ^{3,4,5}, J. Khuyagbaatar^{3,4}, B. Kindler ³, B. Lommel ³, E. C. Simpson¹, C. Sengupta¹, B. M. A. Swinton-Bland ¹, T. Tanaka ¹, A. Yakushev^{3,4}, K. Eberhardt⁵, C. Mokry^{4,5}, J. Runke^{3,5}, P. Thörle-Pospiech^{4,5} and N. Trautmann⁵

¹*Department of Nuclear Physics, Research School of Physics, Australian National University, Canberra, ACT 2601, Australia*

²*Variable Energy Cyclotron Centre, 1/AF-Bidhannagar, Kolkata 700064, India*

³*GSI Helmholtzzentrum für Schwerionenforschung, 64291 Darmstadt, Germany*

⁴*Helmholtz Institute Mainz, 55099 Mainz, Germany*

⁵*Institut für Kernchemie, Johannes Gutenberg-Universität Mainz, 55099 Mainz, Germany*



(Received 10 May 2020; accepted 14 July 2020; published 4 August 2020)

Background: Cross sections for the formation of superheavy elements (SHE) by heavy ion fusion are suppressed by the competing quasifission process. This results in a fissionlike decay after capture but before formation of a compact compound nucleus. Fast quasifission is evident from very mass-asymmetric fission, focused in angle. In contrast, slow quasifission shows no significant mass-angle correlation, and a mass distribution peaked at symmetry. However, it shows angular distributions more anisotropic than those calculated for fission following fusion. Following fusion, low excitation energies should increase SHE survival through reduced competition from fission. However, in reactions with deformed actinide target nuclei, subbarrier fusion is highly suppressed by both fast and slow quasifission.

Purpose: To investigate the threshold for quasifission by investigating signatures of slow quasifission in both fission angular and mass distributions, as a function of beam energy with respect to the capture barrier, for the projectiles ${}^9\text{Be}$, ${}^{12}\text{C}$, and ${}^{16}\text{O}$ that form the neighboring compound nuclei ${}^{258,260}\text{No}$.

Methods: Fission mass and angular distributions have been measured from below to above-barrier energies using the kinematic coincidence method for the reactions ${}^9\text{Be} + {}^{249}\text{Cf}$, ${}^{12}\text{C} + {}^{248}\text{Cm}$, and ${}^{16}\text{O} + {}^{244}\text{Pu}$. Fission following transfer reactions can significantly contaminate fission events that follow capture, and must be rejected. Existing methods to reject transfer-induced fission have been refined to allow quantitative subtraction of the transfer fission component.

Results: The capture-fission mass-angle distributions show no evidence for fast quasifission, as might be expected. However, measured fission fragment angular anisotropies are larger than transition state model (TSM) calculations for fusion fission. The deviations increase with larger projectile charge and for bombarding energies below the mean capture barrier energy. Even for the ${}^9\text{Be} + {}^{249}\text{Cf}$ reaction, the subbarrier angular anisotropy significantly exceeds the TSM calculation. Fission mass distributions measured at the same excitation energies also show a consistent dependence on the projectile charge.

Conclusions: New refined analysis techniques have been developed to enable reliable separation of fission following capture from sequential fission following transfer reactions. For fission following capture at above-barrier energies, the ${}^9\text{Be}$ angular anisotropies are close to the TSM predictions, supporting the validity of TSM calculations of fusion-fission for such heavy elements. At subbarrier energies the angular anisotropy data indicate a component of slow quasifission even for ${}^9\text{Be}$, and a probability that increases rapidly with projectile charge. It is concluded that the probability of slow quasifission changes smoothly with projectile charge, having no sharp threshold.

DOI: [10.1103/PhysRevC.102.024603](https://doi.org/10.1103/PhysRevC.102.024603)

I. INTRODUCTION

For reactions forming heavy and superheavy elements (SHE), the competition between fusion and quasifission following capture plays a major role in determining the reaction outcome. It has been shown experimentally [1,2] that two

distinct categories of quasifission compete with fusion: fast quasifission (FQF) and slow quasifission (SQF). Fast quasifission is generally mass-asymmetric. It shows a correlation of fragment mass with angle, which demonstrates the presence of quasifission events where following contact, the system breaks apart in less than half a rotation of the composite system [3,4], typically corresponding to a sticking time of <10 zeptoseconds (zs) [3,5–7]. Quasifission can also occur on a longer time scale, resulting in fragment masses peaked near mass symmetry. This has been termed slow quasifission

*Presently at Flerov Laboratory of Nuclear Reactions, Joint Institute for Nuclear Research, Dubna 141980, Russia; he.tatha@gmail.com

[2,8] or deep quasifission [9]. It has a smaller or negligible mass-angle correlation, and its observables (e.g., mass and angular distributions) often overlap with those of fusion-fission. Direct evidence for SQF has been obtained from the deviation of measured fission fragment angular distributions [1,2,10] from saddle-point transition state model (TSM) calculations for fusion-fission [10,11].

Independent evidence for QF competition, and SQF in particular, was also obtained through the systematic study of fusion-evaporation cross sections in reactions forming the same compound nucleus [8,12–14].

Following the demonstration of distinct characteristics for the fast and slow quasifission processes [1], more recent work [2] has attempted to quantify the competition between fusion and quasifission in subbarrier reactions with actinide target nuclei. It has been shown experimentally that the contributions of slow quasifission [1,15–17] and fast quasifission [1,2,6,7] increase at subbarrier energies. From the outset, this was associated with the effect of deformation alignment of the statically deformed actinide nuclei [15], as explained below.

At subbarrier energies the only collisions resulting in capture are those where the deformation axis of the actinide nucleus is aligned with the approaching projectile. This results in a lower capture barrier, and is associated with an elongated composite system after capture. This has been related to changes in both the probability and characteristics (time scale) of the quasifission processes [6,15,16].

Langevin dynamics calculations that were matched to experimental mass distributions [18] led to suggestions that despite this deformation alignment effect, the production of SHEs in collisions at subbarrier energies should be pursued. The question is whether the predicted quasifission probabilities (and thus SHE cross sections) are correct. This will be determined by whether the slow quasifission process, resulting in near-symmetric fission decays, has a larger probability than model calculations predict, and thus results in a larger suppression of the cross sections for formation of a compact compound nucleus, and thus of SHEs. In Ref. [2], a rapid increase in the probabilities of fast quasifission (P_{FQF}) and slow quasifission (P_{SQF}) with increasing projectile charge was inferred for subbarrier collisions, the transition being centered around projectile atomic number $Z_P \approx 14$ for P_{FQF} and $Z_P \approx 8$ for P_{SQF} .

Taking fast quasifission and the slow quasifission to be sequential processes, rather than simultaneous, the fusion probability (P_{CN}) has been proposed [2] to be the *product* of the probability of surviving each process:

$$P_{\text{CN}} = (1 - P_{\text{FQF}})(1 - P_{\text{SQF}}). \quad (1)$$

For reactions of projectiles heavier than $Z = 16$ with actinide nuclei, it was concluded [2] that the probability of forming SHEs at below-barrier energies appears unfavorable. However, this could possibly be offset by a significantly increased fission survival probability due to the compound nucleus (CN) being formed at lower excitation energies. To be able to accurately predict SHE cross sections, it is important to understand both the dependence of P_{FQF} and P_{SQF} on entrance channel parameters (e.g., charge product, beam energy and the

nuclear structure of the colliding nuclei), and to understand the physical variables controlling these dependencies.

This experimental investigation aims to increase our knowledge of the systematics of subbarrier slow quasifission probabilities in reactions with prolate deformed actinide nuclei. This should aid in testing theoretical models, and thus in obtaining more reliable predictions of SHE cross sections at subbarrier energies.

In the present work, to investigate the dependence of the probability of slow quasifission on the entrance channel conditions, six mass-asymmetric reactions with actinide target nuclei have been chosen, where the probability of fast quasifission is expected to be negligible.

The main focus of this investigation is on the reactions ${}^9\text{Be} + {}^{249}\text{Cf}$, ${}^{12}\text{C} + {}^{248}\text{Cm}$, and ${}^{16}\text{O} + {}^{244}\text{Pu}$, which populate the compound nuclei ${}^{258,260}\text{No}$. By forming the same or nearby compound nuclei with similar excitation energies and angular momenta, differences in the observed fission characteristics can be attributed to changes in the contributions from quasifission. Additionally, measurements were made for ${}^9\text{Be} + {}^{238}\text{U}$, ${}^{244}\text{Pu}$, and ${}^{248}\text{Cm}$.

Fission following transfer reactions can interfere with measurements of fission following capture in reactions with actinide nuclei. The reason is the low fission barriers of the heavy transfer products. This can be a very significant problem at subbarrier energies, where the cross sections for transfer reactions can be much larger than for capture, as demonstrated for the reaction ${}^{19}\text{F} + {}^{232}\text{Th}$ [2]. To obtain accurate experimental data, the contribution from fission following transfer reactions must be separated from fission following capture of the full projectile mass (or momentum), known as full momentum transfer (FMT) fission. A new approach was developed in this work to optimize quantitative determination of the characteristics of the FMT fission.

Fission from the reactions of ${}^{16}\text{O}$, ${}^{12}\text{C}$, and ${}^9\text{Be}$ with ${}^{204,208}\text{Pb}$ and/or ${}^{197}\text{Au}$ targets were also measured to provide a reference with no transfer-fission.

II. EXPERIMENTAL DETAILS

The measurements were carried out at the Heavy Ion Accelerator Facility (HIAF) of the Australian National University. Beams of ${}^9\text{Be}$, ${}^{12}\text{C}$, and ${}^{16}\text{O}$ were used, with the range of energies given in Table I. For each projectile and beam energy measurement with the actinide targets, a reference measurement was made on a Pb target, for which fusion-fission should be by far the predominant fission outcome. The use of pulsed beams, with width ≈ 1 ns and pulse separation of 107 ns, was essential to allow the event-by-event determination of the velocity of the fissioning nucleus. This allowed separation of the fission components resulting from capture-fission and from transfer-fission, as described in Sec. III.

Targets of ${}^{244}\text{Pu}$, ${}^{248}\text{Cm}$, and ${}^{249}\text{Cf}$, enriched to levels $>97\%$, were produced at the Johannes Gutenberg University Mainz by molecular plating [19,20] from organic solution (isobutanol/isopropanol). The target diameter was 3 mm. Backing foils for these targets comprising 230–250 $\mu\text{g}/\text{cm}^2$ Al with a 29–39 $\mu\text{g}/\text{cm}^2$ coating of Ti were fabricated at the GSI target laboratory. Before colliding with the transuranium

TABLE I. Reaction parameters for the measurements presented in this work, including the identity of the compound nucleus (CN) formed in complete fusion. The center of mass energy ($E_{c.m.}$) is the mean energy in the middle of the transuranium layer of the target. The quoted Al backing thickness is the thickness of Al equivalent in energy loss to the double-layer backing of Al with a thin Ti coating (see text). V_B are the calculated capture barriers of Broglia and Winther [25].

Beam	Target ($\mu\text{g}/\text{cm}^2$)	Actinide areal density ($\mu\text{g}/\text{cm}^2$)	Upstream foil $^{\text{nat}}\text{C}$ ($\mu\text{g}/\text{cm}^2$)	Downstream backing		CN	E_{lab} (MeV)	$E_{c.m.}$ (MeV)	V_B (MeV)
				$^{\text{nat}}\text{C}$ ($\mu\text{g}/\text{cm}^2$)	^{27}Al ($\mu\text{g}/\text{cm}^2$)				
$^{16}_8\text{O}$	$^{244}_{94}\text{Pu}$	50	38	—	275	$^{260}_{102}\text{No}$	84.90–116.27	79.54–109.01	84.82
$^{12}_6\text{C}$	$^{248}_{96}\text{Cm}$	44	38	—	291	$^{260}_{102}\text{No}$	60.80–89.18	57.91–84.96	66.05
^9_4Be	$^{249}_{98}\text{Cf}$	34	38	—	318	$^{258}_{102}\text{No}$	45–60	43.32–57.82	45.73
^9_4Be	$^{248}_{96}\text{Cm}$	44	38	—	291	$^{257}_{100}\text{Fm}$	45–60	43.36–57.85	44.83
^9_4Be	$^{244}_{94}\text{Pu}$	50	38	—	275	$^{253}_{98}\text{Cf}$	45–60	43.36–57.84	44.03
^9_4Be	$^{238}_{92}\text{U}$	60	—	12	—	$^{247}_{96}\text{Cm}$	45–60	43.33–57.79	43.28

targets, beam ions passed through a thin carbon foil to reduce sputtering of target materials. Details including the effective thickness of target materials is given in Table I. The reference targets of Pb ranged in thickness from 55 to 220 $\mu\text{g}/\text{cm}^2$ on 18 to 33 $\mu\text{g}/\text{cm}^2$ carbon backing foils. The effect of energy loss of fission fragments in the targets (and more significantly in the backings) was minimized by (i) having the target backings facing downstream, where the fission fragment velocities are higher, and (ii) placing the target normal at 60° to the beam axis. Energy losses of the beam particles and fission fragments in the target materials were iteratively corrected event-by-event, assuming the reaction occurred in the center of the transuranium layer. Energy losses in targets and backings were checked through an analysis of the energy spectra of α particles originating from the radioactive decay of the target isotopes, measured in a Si detector calibrated with an open “triple- α ” source.

The fission fragments were detected using the CUBE spectrometer, consisting in these experiments of three multiwire proportional counters (MWPCs) arranged as shown in Fig. 1. The red arrow indicates the beam axis, the beam diameter on the target being ≤ 1 mm FWHM. While MWPC-2 covered the forward laboratory angles, MWPC1 and MWPC3 covered angles 50° – 168° , detecting the complementary fission fragment. The active areas of MWPC-1 and -2 are 279×357 mm 2 . MWPC-3 has an area of 131×357 mm 2 . Two silicon surface barrier detectors (labeled Monitor-1 and Monitor-2) were placed at laboratory angles of $\theta = 22.5^\circ$ and $\phi = 90^\circ$, 270° to measure elastically scattered events for beam and target monitoring, and absolute cross-section normalization.

Data collection of events in the MWPC detectors was generally triggered by a coincidence between a signal in the forward detector and in one of the backward detectors. For these light beams, the electronic thresholds could be set to discriminate against scattering events without cutting fission events. Thus, the recorded events were almost exclusively fissions. For position calibration measurements using a ^{60}Ni beam and the spontaneous fission of ^{248}Cm , the data were collected in singles mode, i.e., self-triggered by each MWPC. Position information was extracted from the X and Y anode planes of each MWPC, which are made up of a grid of 20 μm gold-plated tungsten wires spaced by 1 mm. The center foil of

0.9 μm Au-coated polyethylene terephthalate provided timing and energy loss information. From the position information, the angles of the detected fragments (θ , ϕ) were calculated. Fission fragment velocities, energies and mass ratios (M_R) were calculated in the center-of-mass frame from the time-of-flight and angle information using momentum and mass conservation [16,21]. The effect of event losses due to electronic dead-time for both the MWPCs and monitors [22] were taken into account in the analysis to determine differential cross-sections ($d^2\sigma/dM_R d\theta_{c.m.}$), where $\theta_{c.m.}$ is the scattering angle of the fragment in the center of mass frame.

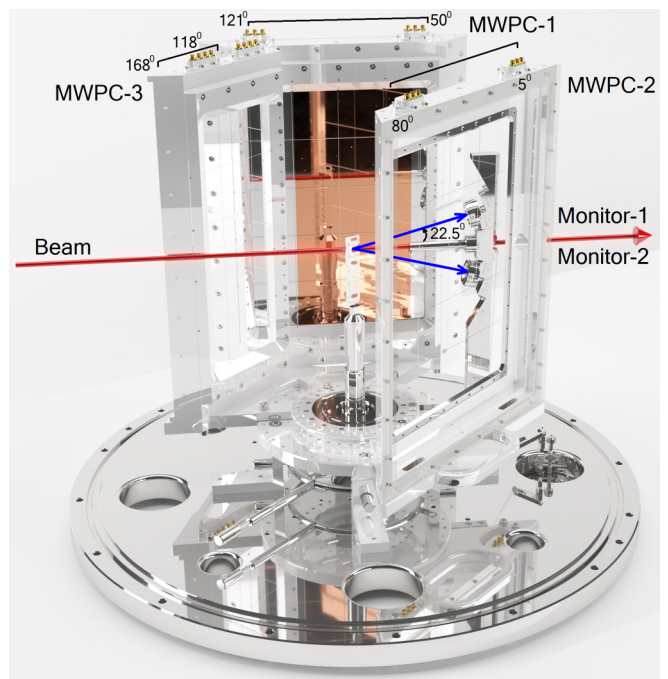


FIG. 1. Computer rendering of the CUBE detector setup for these experiments. The backing plate and internal elements of MWPC2 and MWPC3 have been rendered transparent for clarity. The two Si monitor detectors have a scattering angle from the target of 22.5° .

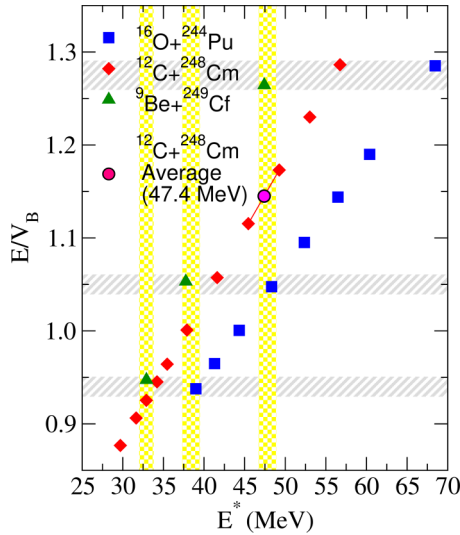


FIG. 2. Compound nucleus excitation energies E^* and E/V_B values for the reactions $^{16}\text{O} + ^{244}\text{Pu}$, $^{12}\text{C} + ^{248}\text{Cm}$ and $^9\text{Be} + ^{249}\text{Cf}$. The points in the vertical (yellow) bands represent the measurements selected for comparison with similar E^* . The circular magenta point at $E^* = 47.4$ MeV is the average of the 45.5 and 49.3 MeV points for the $^{12}\text{C} + ^{248}\text{Cm}$ reaction, which matches more closely the excitation energies for the other two reactions. The points within the horizontal gray shaded bands are those selected for comparison with similar E/V_B , namely, ≈ 0.94 , ≈ 1.05 , and ≈ 1.28 .

III. ANALYSIS AND RESULTS

The description of the analysis of these experimental data focuses on the three reactions $^9\text{Be} + ^{249}\text{Cf}$, $^{12}\text{C} + ^{248}\text{Cm}$ and $^{16}\text{O} + ^{244}\text{Pu}$, which populate the compound nuclei $^{258,260}\text{No}$. The fusion-fission, transfer-fission, and quasifission relative probabilities and characteristics are expected to depend on both the compound nucleus excitation energy (E^*) and the ratio of the beam energy to the average capture barrier energy E/V_B . E^* for each reaction are shown in Fig. 2, plotted against the corresponding value of E/V_B . To simplify the presentation of experimental results, the measurements with approximately matching E^* and E/V_B have been selected for display in subsequent figures. The data at matching E/V_B lie in the gray-shaded bands, while those at matching E^* lie in the yellow shaded bands. The circular magenta point shows the average E^* for $^{12}\text{C} + ^{248}\text{Cm}$ of the two points on either side, where these measured mass distributions have been averaged to obtain a closer match in E^* to the other reactions.

A. Fission source velocity analysis

The use of pulsed beams allowed event-by-event determination of the components of the fissioning nucleus (fission source) velocity vectors in the laboratory frame, both parallel (v_{\parallel}) and perpendicular (v_{\perp}) to the beam axis, using the equations described in Ref. [16]. For a true binary event, momentum conservation leads to the expectation that v_{\parallel} should be equal to the center-of-mass velocity (v_{CN}), and v_{\perp} should be zero.

The process of fission generally involves the evaporation of several light particles, principally neutrons, which can be emitted before or after scission. Thus, the fission process is not strictly binary. This will perturb the deduced fission source velocity vectors. For isotropic emission, the mean values of v_{\parallel} and v_{\perp} should be unchanged, but each will show a distribution about these values, whose width will depend on the multiplicity and momentum distribution of the evaporated particles.

In the case of a transfer reaction triggering fission, a beam-like particle will be ejected, carrying much more momentum than a neutron. Thus, the values of v_{\parallel} and v_{\perp} will be perturbed much more than in fusion-fission. Since transfer reactions occur at a limited range of angles around the grazing angle (rather than isotropically), the distribution of v_{\parallel} will generally not be distributed symmetrically around v_{CN} .

To present experimental data most clearly, it is useful to show a matrix of the quantity $[v_{\parallel} - v_{\text{CN}}]$ against v_{\perp} , where FMT fission (capture fission) is expected to be centered at (0,0), and transfer-induced fission events should generally lie away from this point. The panels (a)–(c) in the top row in Fig. 3 shows such plots for the reaction $^{16}\text{O} + ^{244}\text{Pu}$ at $E/V_B = 1.28$, for three angular ranges ($\theta_{\text{c.m.}} = 95^{\circ}\text{--}105^{\circ}$, $125^{\circ}\text{--}140^{\circ}$, $150^{\circ}\text{--}160^{\circ}$). The FMT fission events are the high intensity group centered at (0,0). The transfer-fission events are the diffuse groups displaced from (0,0). The right-hand panel [Fig. 3(d)] is for the $^{16}\text{O} + ^{204}\text{Pb}$ reaction, where transfer-fission is not expected, and indeed only the FMT fission group centered at (0,0) is seen.

The figure shows that moving backward in c.m. angle results in the FMT source velocity distributions making a transition from a circular distribution near $\theta_{\text{c.m.}} = 90^{\circ}$ to increasingly elliptical ones at more backward angles. It was found that this is the combined effect of deviations of both v_{\parallel} and v_{\perp} from their values expected for purely binary events. This could be accounted for, allowing us to achieve a more consistent extraction of the FMT fission component as a function of angle. For small deviations of v_{\parallel} from v_{CN} , this trend is corrected by taking the deduced value of $[v_{\parallel} - v_{\text{CN}}]$ determined according to Ref. [16], and multiplying by $\sin\theta_{\text{c.m.}}$. Further explanation is given in Appendix, where it is demonstrated that the increasingly elliptical distributions result from the recoil velocity component out of the fission plane.

Distributions of $[v_{\parallel} - v_{\text{CN}}]\sin\theta_{\text{c.m.}}$ versus v_{\perp} are shown in the lower panels of Fig. 3. The FMT fission distributions (centre) no longer show a transition to elliptical shapes with increasing angle, remaining almost perfectly circular, as expected for essentially isotropic neutron evaporation. These spectra with the event-by-event multiplication by $\sin\theta_{\text{c.m.}}$ will henceforth be referred to as $[v_{\parallel} - v_{\text{CN}}]$ distributions.

With this refinement to the fission source velocity reconstruction procedure, scatter plots of the measured $[v_{\parallel} - v_{\text{CN}}]$ (including the $\sin\theta_{\text{c.m.}}$ factor) against v_{\perp} were generated for all angle bins, for all the reactions under investigation. Examples of such experimental results for the reactions $^{16}\text{O} + ^{244}\text{Pu}$, $^{12}\text{C} + ^{248}\text{Cm}$ and $^9\text{Be} + ^{249}\text{Cf}$ are presented in Fig. 4 for the angle bin $95^{\circ} < \theta_{\text{c.m.}} < 105^{\circ}$. Each row corresponds to

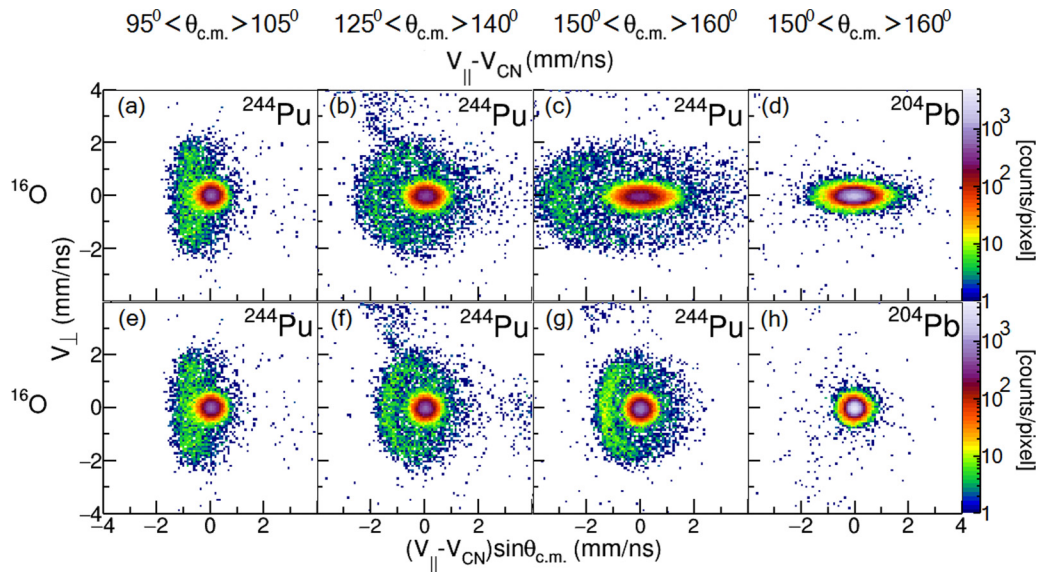


FIG. 3. The top panels (a)–(d) show the reconstructed fission source velocity distributions in $[v_{\parallel} - v_{\text{CN}}]$ and v_{\perp} (see text) for the $^{16}\text{O} + ^{244}\text{Pu}$ and $^{16}\text{O} + ^{204}\text{Pb}$ reactions within the indicated angular ranges. In the bottom panels (e)–(h), $[v_{\parallel} - v_{\text{CN}}]$ has been multiplied event-by-event by $\sin\theta_{\text{c.m.}}$, which eliminates the change in shape of the central FMT fission group with angle (see text). The events distributed beyond the FMT peaks for $^{16}\text{O} + ^{244}\text{Pu}$ results from fission following transfer reactions; these are absent for $^{16}\text{O} + ^{204}\text{Pb}$.

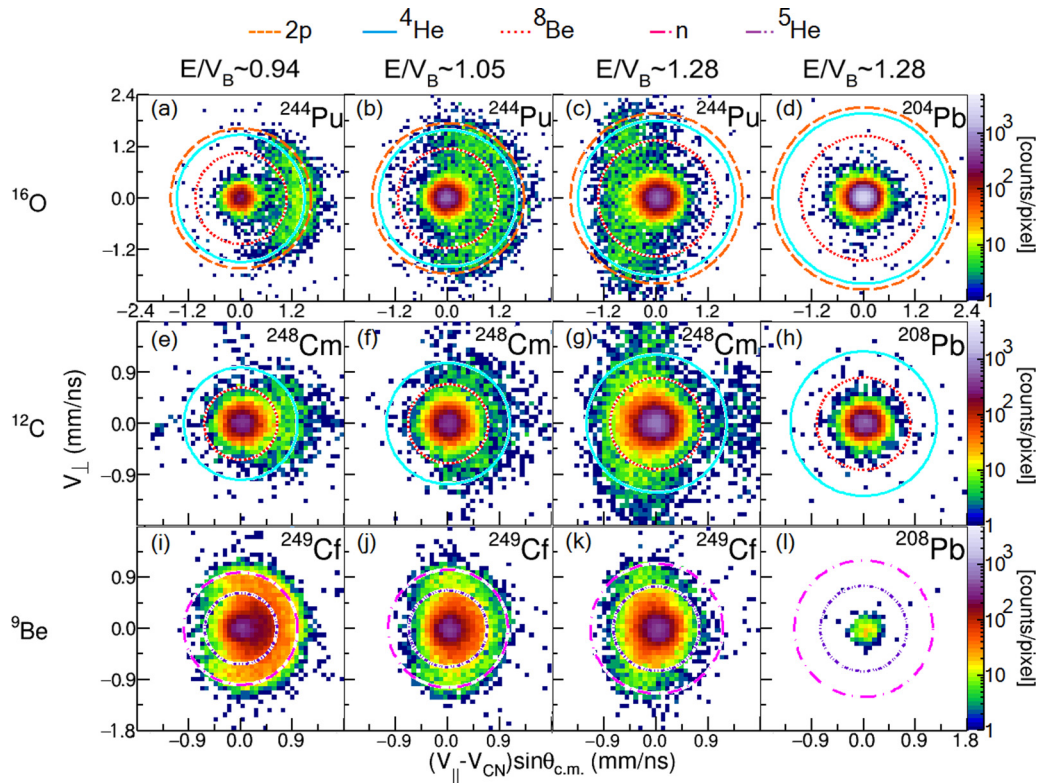


FIG. 4. Plots of the fission source velocity distributions (with event-by-event $\sin\theta_{\text{c.m.}}$ scaling as described in the text) for the reactions $^{16}\text{O} + ^{244}\text{Pu}$, $^{12}\text{C} + ^{248}\text{Cm}$, and $^9\text{Be} + ^{249}\text{Cf}$ at approximately matching values of E/V_B as indicated (blue bands in Fig. 2). The angular range is $95^\circ < \theta_{\text{c.m.}} < 105^\circ$. Data for the indicated Pb targets are also shown, contrasting with the actinide targets in having essentially no transfer-fission. The colored rings show the calculated boundaries for fission following the specific (projectile stripping) transfer reactions as indicated (top), which are expected to give the highest excitation energies in the heavy recipient nucleus, and thus be the most likely to result in subsequent fission.

a given projectile, while each column corresponds to similar E/V_B . Here the V_B are calculated using the prescription given in Ref. [25] and are listed in Table I. The fourth column of Fig. 4 is for reactions with Pb targets, measured as a reference for each projectile and beam energy. Having essentially no transfer-fission (because of the high fission barriers of nuclei close to ^{208}Pb), and with cross sections having previously been measured, they provided a good check of the analysis procedures.

The FMT fission events are essentially described by a two-dimensional Gaussian function centered at (0, 0). For isotropic evaporation, this distribution would be exactly symmetric. The surrounding transfer-fission events however show a complex dependence on both projectile and beam energy. As expected, for the Pb reactions, there is essentially no evidence for transfer-fission.

For the actinide targets, transfer-fission makes a significant contribution. For these events, the absolute magnitude of the typical offset in velocity space from $([v_{||} - v_{\text{CN}}], v_{\perp}) = (0, 0)$ can be calculated as follows. In order for fission to occur following transfer, the excitation energy of the heavy transfer product should be higher than the fission barrier, typically 6 MeV. Thus, the transfer kinematics can be calculated for a given transfer reaction leading to a minimum of 6 MeV excitation energy in the heavy product. The velocity v_{tr} of the heavy transfer reaction product in the center-of-mass reference frame ($v_{\text{tr}} = v_{\text{recoil}} - v_{\text{CN}}$) can then be determined from simple kinematics. v_{tr} is independent of the transfer center-of-mass angle. Thus, if the transfer angular distribution were isotropic, then the heavy nucleus recoil velocity vector distribution would comprise a spherical shell of radius v_{tr} , centered at $v_{||} = v_{\text{CN}}$ and $v_{\perp} = 0$, equivalent to $([v_{||} - v_{\text{CN}}], v_{\perp}) = (0, 0)$.

Experimentally only two fission source velocity components can be determined: (i) that parallel to the beam and (ii) that perpendicular to both the beam axis and the fission axis [16]. The spherical shell when projected onto these two variables results in a distribution bounded by a circle of radius v_{tr} , with peak yield at v_{tr} , and a minimum yield within that limit at (0, 0).

Although the dependence of the transfer probability on azimuthal angle would be expected to be essentially isotropic, the distribution in scattering angle certainly should not be. This is reflected in the experimental data. At the lowest energies, the mean $[v_{||} - v_{\text{CN}}]$ for transfer-fission events is positive, corresponding to a projectilelike nucleus recoiling to backward angles, associated with a grazing angle of

$\approx 180^\circ$. At the highest energy, the mean $[v_{||} - v_{\text{CN}}]$ is negative, corresponding to a grazing angle $< 90^\circ$. At $E/V_B \approx 1.05$, the transfer-fission source velocity distribution is intermediate between these extremes.

The probability of fission of the heavy transfer product will increase with increasing E^* above the fission barrier (≈ 6 MeV). Thus, the contribution from a given transfer reaction will depend on the probability of the transfer, and the distribution of E^* , which will extend to high energies. The value of E^* corresponding to the kinematically optimal Q value for transfer [23,24,26] (Q_{opt}) should thus give a good measure of the likelihood of fission. This ‘‘optimum transfer excitation energy’’ E_{opt}^* can be calculated from the difference between the ground state Q value Q_{gg} and Q_{opt} : $E_{\text{opt}}^* = Q_{\text{gg}} - Q_{\text{opt}}$.

For the reactions $^{16}\text{O} + ^{244}\text{Pu}$, $^{12}\text{C} + ^{248}\text{Cm}$ and $^9\text{Be} + ^{249}\text{Cf}$, Table II shows E_{opt}^* (in MeV) for transfer of one neutron (n), two protons ($2p$), an α particle (^4He) and ^5He , and (in relevant reactions) ^8Be transfer. In general the stripping reactions lead to much higher E^* , as expected from the Coulomb term in the expression [23,24] for Q_{opt} .

The transfer reactions most likely to result in fission for the $^{16}\text{O} + ^{244}\text{Pu}$ reaction are $2p$, ^4He and ^8Be stripping. For $^{12}\text{C} + ^{248}\text{Cm}$ they are ^4He and ^8Be stripping, and for the $^9\text{Be} + ^{249}\text{Cf}$ reaction, neutron (n) and ^4He , ^5He stripping. The values of v_{tr} have been calculated for these transfers, and are shown in Fig. 4 by the identified circles plotted over the experimental data. These represent the maximum deviation from (0, 0) for each transfer channel, neglecting the spreading from subsequent neutron evaporation from the fission fragments. The larger fission probability with increasing excitation energy above 6 MeV should result in most transfer-induced fission events lying inside these limits. However, the further spreading of the experimental distributions due to neutron evaporation, that can occur both before and after scission, is expected to result in some events extending outside the calculated limits.

The experimental data show good consistency with these expectations. The results for $^9\text{Be} + ^{249}\text{Cf}$ are of particular interest, since the largest relative yield of transfer fission would be expected for this reaction. This is because ^9Be is weakly bound. Transfer-fission should be most prominent at subbarrier energies, where FMT fission is suppressed by the requirement that the whole projectile tunnels through the potential barrier. Figure 4(i) shows the experimental fission source velocity distribution at $E/V_B = 0.94$. The pink

TABLE II. Optimum transfer excitation energies E^* in MeV for projectile stripping and pickup [23,24] for the reactions $^{16}\text{O} + ^{244}\text{Pu}$, $^{12}\text{C} + ^{248}\text{Cm}$, and $^9\text{Be} + ^{249}\text{Cf}$. Values of E^* are given for transfer of a neutron (n), two protons ($2p$), ^4He and ^5He , and stripping of ^8Be for the heavier projectiles. The reactions with the most positive E^* are most likely to result in fission of the heavy transfer product.

Systems	Optimum stripping E^*					Optimum pick-up E^*			
	n	$2p$	^4He	^5He	^8Be	n	$2p$	^4He	^5He
$^{16}\text{O} + ^{244}\text{Pu}$	-10.89	+9.50	+7.75	-6.26	+15.15	-1.88	-28.02	-9.76	-8.93
$^{12}\text{C} + ^{248}\text{Cm}$	-14.01	+5.08	+7.88	-6.21	+23.34	-1.27	-26.54	-8.21	-10.09
$^9\text{Be} + ^{249}\text{Cf}$	+4.96	+1.91	+13.28	+20.68	-	+1.23	-17.09	-5.04	-2.38

long-dashed line shows the calculated boundary for neutron transfer induced fission, where a ^8Be projectilelike nucleus recoils. Experimentally a semi-circular distribution extending out to the calculated circle is seen, with mean $[v_{\parallel} - v_{\text{CN}}] > 0$, corresponding to the projectilelike nucleus recoiling backward of 90° , as expected at a subbarrier energy. Inside this is the purple-dot-dashed circle corresponding to the calculated boundary for transfer of ^5He , with a ^4He recoiling. The experimental data show a concentration of events inside this boundary, again with $[v_{\parallel} - v_{\text{CN}}] > 0$. In this case the events correspond to center-of-mass angles backwards of $\approx 120^\circ$. The difference in behavior of transfer of a neutron and of ^5He is consistent with the transfer of ^5He requiring a smaller inter-nuclear separation than transfer of the weakly bound neutron. The FMT fission events are clearly centered at $(0, 0)$, but for this reaction, it appears that there will be some overlap with fission following ^5He transfer.

B. Obtaining FMT fission cross sections

The FMT fission group is quite well-separated from the transfer-fission events for the $^{16}\text{O} + ^{244}\text{Pu}$ reaction, but as noted, for the $^9\text{Be} + ^{249}\text{Cf}$ reaction the two components overlap. In principle, to select FMT events with minimal transfer-fission contamination, it should be sufficient to apply a circular gate with very small radius centered at $(0, 0)$, since the FMT fission yield is maximal, and transfer-fission minimal at this point. This approach was used to investigate the FMT mass distributions, as presented in Sec. III 2. However, to determine the cross section of FMT fission as a function of angle, the total yield of FMT fission must be determined, requiring subtraction of the overlapping transfer-fission events. To achieve this in a quantitative way, a new approach was developed, fitting FMT and transfer-fission components in both $[v_{\parallel} - v_{\text{CN}}]$ and v_{\perp} .

To assist in understanding this procedure, Fig. 5 shows schematically the three sources of fission events. The central red circle represents the FMT fission, and the dark blue represents the peak in yield of the transfer-fission events that results from the projection of the spherical velocity shells onto two dimensions (see Appendix B). Finally the pale blue region represents the transfer-fission contribution inside the boundary region, which results from azimuthal angles of transfer closer to the fission plane (referred to subsequently as azimuthal transfer fission). Assuming all azimuthal angles are equally likely, this (pale blue) yield can be calculated based on the dark blue yield, as described in Appendix B, allowing subtraction of the transfer fission events from the FMT fission events in any given gate around $(0, 0)$. The transfer-fission subtraction procedure comprised three stages, which are described below.

The first step was to apply cuts on v_{\perp} to exclude the FMT fission events, as illustrated in Fig. 5(b). The x -projection results in the transfer-fission yields over the range of $[v_{\parallel} - v_{\text{CN}}]$ where the FMT events are present. Using the known gate limits applied to v_{\perp} , the contribution of transfer-fission present in the region around $v_{\perp} = 0$ where the FMT fission events lie could then be obtained. The factor by which the gated transfer yield should be scaled, depends on $[v_{\parallel} - v_{\text{CN}}]$,

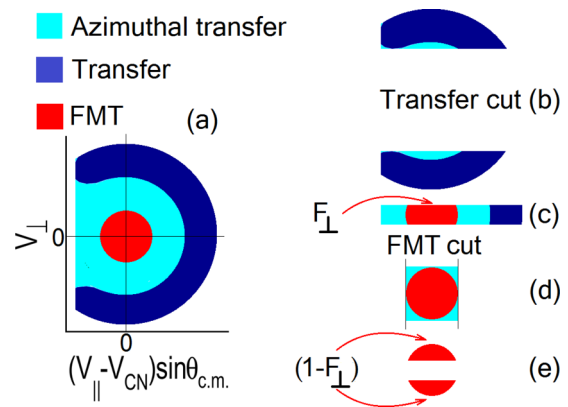


FIG. 5. (a) Schematic diagram of three sources of fission having kinematically different origins: (i) FMT fission following complete fusion (red circle); (ii) the intense group resulting from fission following a transfer reaction far from the plane of the subsequent fission (dark blue arc) and (iii) the more spread-out fission events following a transfer reaction closer to the plane of the subsequent fission (given the label “azimuthal transfer”). The different cuts on the data used in the determination of the FMT fission cross sections is shown in panels (b), (c), (d), as described in the text. The FMT fissions not included in cut (c) comprise $(1-F_{\perp})$ of all FMT fissions, as shown in panel (e) (see text).

and is described in detail in Appendix B. The factor is always $\ll 1$, as demonstrated in Fig. 18 of Appendix B.

The second step was to apply a narrow cut around $v_{\perp} = 0$ to preferentially select FMT fission events, as illustrated in Fig. 5(c). The effect of the width of the cut was accounted for in the analysis, as described below. In practice the width of the applied gate in v_{\perp} was chosen to be $\pm\sigma_{v_{\perp}}$, the standard deviation of the Gaussian fitted to the FMT v_{\perp} distribution for the reaction on the Pb target, which were measured for each beam energy. The resulting $[v_{\parallel} - v_{\text{CN}}]$ spectra contained three components: (i) the FMT fissions centred at $[v_{\parallel} - v_{\text{CN}}] = 0$, (ii) the transfer-fission peaks either at $[v_{\parallel} - v_{\text{CN}}] < 0$ (for $E/V_B \gg 1$) or $[v_{\parallel} - v_{\text{CN}}] > 0$ (for $E/V_B < 1$), and (iii) the contribution from azimuthal transfer fission, which had already been determined in the previous step.

Examples of these experimental spectra of $[v_{\parallel} - v_{\text{CN}}]$ are shown in Fig. 6, for $95^\circ < \theta_{\text{c.m.}} < 105^\circ$ and for the same reactions and energies as shown in Fig. 4. These spectra were fitted with the azimuthal transfer fission component (purple dot-dashed curve) fixed from the previous step, one unconstrained Gaussian for the FMT fission component (green dot-dashed Gaussian), and one or more Gaussians for the transfer-fission (red dashed Gaussians). Overall, the total fits to the distributions, indicated by the orange curves, are very good. Thus, the area (counts) of the FMT peak ($N_{\text{FMT}}^{\text{cut}}$) for the cuts applied was obtained. However, this area does not yet represent the total FMT yield, due to the narrow cut in v_{\perp} , as illustrated in Fig. 5(c).

The third step of the analysis was to determine the fraction of FMT events $(1-F_{\perp})$ [see Fig. 5(e)] that have been excluded by the narrow gate in v_{\perp} , as illustrated in Fig. 5(c). To achieve this, a cut in $[v_{\parallel} - v_{\text{CN}}]$ was applied around $[v_{\parallel} - v_{\text{CN}}] = 0$ between -0.6 mm/ns and 0.6 mm/ns such that essentially

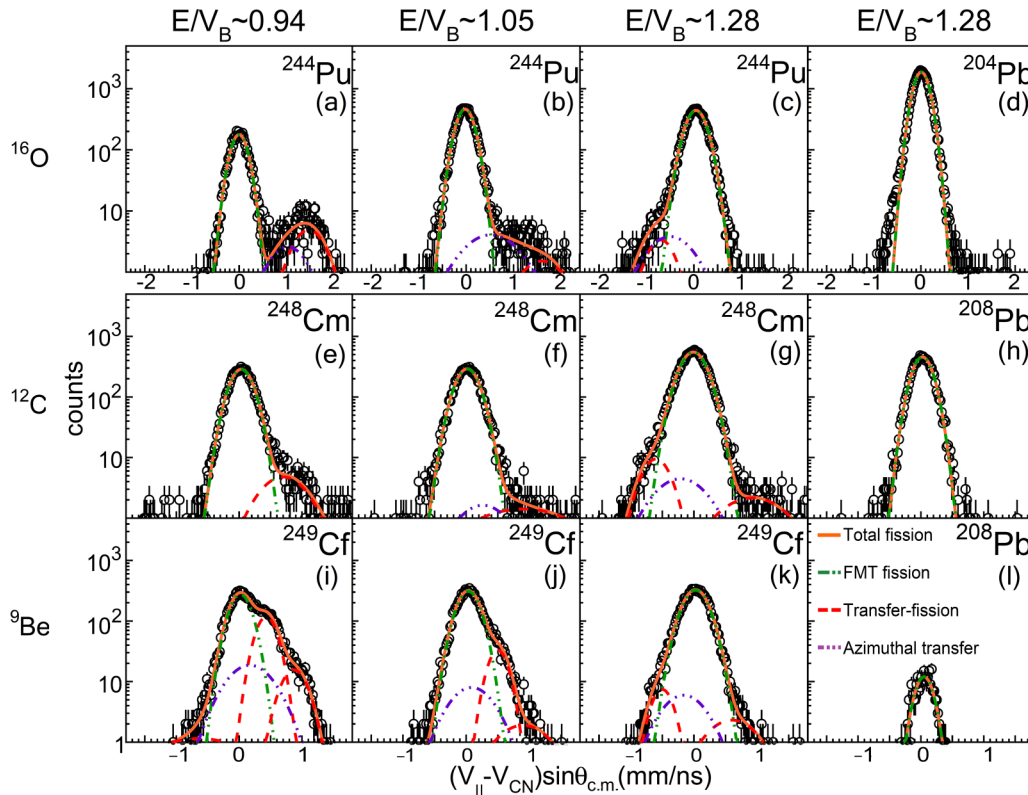


FIG. 6. Spectra of $[v_{||} - v_{CN}]$ with event-by-event $\sin\theta_{c.m.}$ scaling are shown for the same reactions as in Fig. 4. A narrow gate around $v_{\perp}=0$, as illustrated in Fig. 5(c), was applied favoring the FMT fission events (see text). The spectra have been fitted (orange curve) including the defined azimuthal fission component (purple dot-dashed curve), and Gaussians representing FMT fission (green) and transfer-fission (red). The FMT fission component was used to obtain the FMT fission cross sections (see text).

all FMT events were included, as illustrated in Fig. 5(d). The resulting v_{\perp} spectra are shown in Fig. 7. These were then fitted with Gaussians, one central peak corresponding to FMT fission (green dot-dashed curve), and one or more pairs of Gaussians having the same width and height (red dashed curves), symmetrically located about the FMT Gaussian. These Gaussians describe the transfer-fission components, and are required in the fit to obtain the correct width of the FMT Gaussian. From these fits the standard deviations of the FMT Gaussians were determined. Values of F_{\perp} were then determined according to the following equation:

$$F_{\perp} = \frac{\int_{-v_{\perp,FMT}^{\sigma_{Pb}}}^{v_{\perp,FMT}^{\sigma_{Pb}}} \text{FMT-Gaussian-fit}}{\int_{v_{\perp}^{-\infty}}^{v_{\perp}^{\infty}} \text{FMT-Gaussian-fit}} = 0.5 * \left[\text{erf}\left(\frac{v_{\perp,FMT}^{\sigma_{Pb}} - \mu}{\sqrt{2} * \sigma}\right) - \text{erf}\left(\frac{-v_{\perp,FMT}^{\sigma_{Pb}} - \mu}{\sqrt{2} * \sigma}\right) \right], \quad (2)$$

where erf is the error function and μ is the RMS value of the FMT peak of the v_{\perp} spectra in Fig. 7. The total FMT yield (N_{FMT}) was then obtained from

$$N_{\text{FMT}}^{\text{total}} = \frac{N_{\text{FMT}}^{\text{cut}}}{F_{\perp}}. \quad (3)$$

The measurements for the reactions with the Pb targets show slight deviations from the Gaussian fits in the tails of the distributions [see Figs. 7(d) and 7(h)]. This may be a

result of a small component of charged particle evaporation from the compound nucleus prior to fission, which perturbs the two-body kinematics more than neutron evaporation. There may also be a contribution from angular straggling in the targets. The deviation is at a very low level ($\approx 1\%$ of the height of the Gaussian), indicating that characterization of the FMT fissions by a Gaussian distribution is a good approximation.

For the actinide reactions, the contributions from transfer-fission in the region of the FMT peak for the ^{12}C and ^{16}O measurements are very small. This can be seen in Fig. 6, where the transfer-fission components (purple dot-dashed and red dashed curves) are below $\approx 1\%$ of the height of the FMT fission peak. Thus, uncertainties in the transfer-fission subtraction are likely to have negligible effect. The contributions of transfer-fission for the ^9Be measurements are larger, and as expected are maximal at the subbarrier energy. Even here, the transfer-fission yield is not much more than 5% of the peak yield for FMT fission, thus even a 20% uncertainty in the transfer-fission subtraction would only result in $\approx 1\%$ change in FMT yield. At above-barrier energies, the transfer-fission component is of course smaller, being less than 2.5% of the peak FMT yield.

Through the precise experimental data and newly developed subtraction procedures, uncertainties in the FMT characteristics due to the presence of transfer-fission have been reduced to a low level.

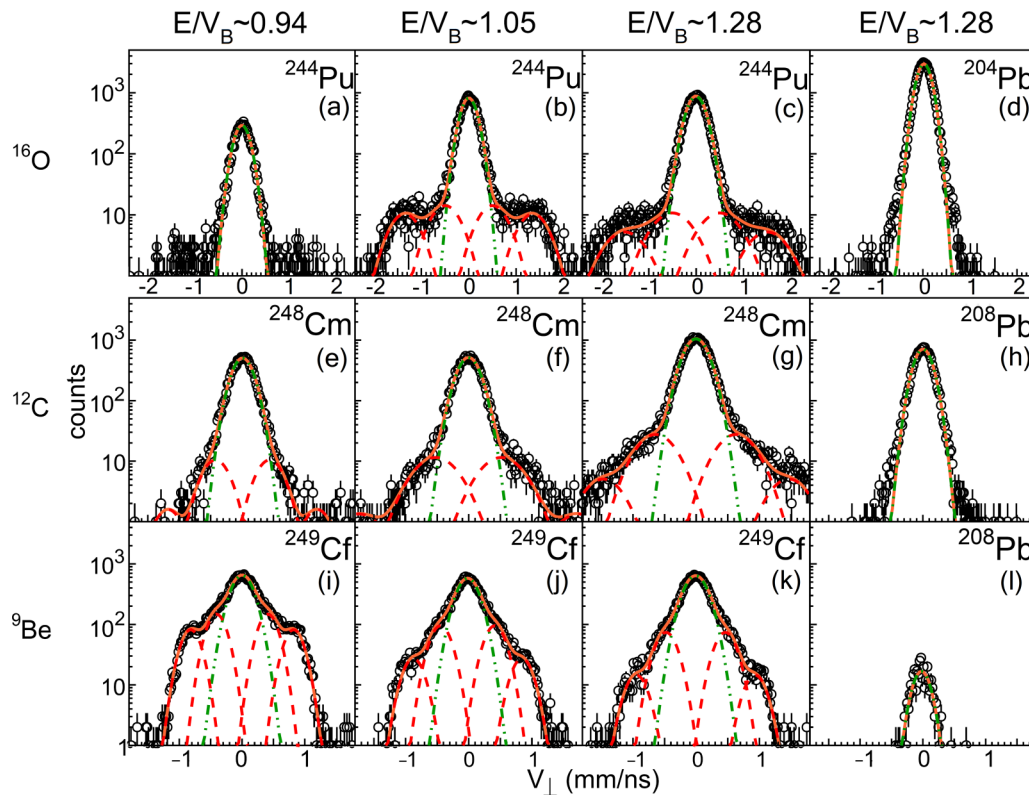


FIG. 7. Spectra of v_{\perp} are shown for the same reactions as in Fig. 4. A gate around $[v_{\parallel} - v_{\text{CN}}]=0$ (orthogonal to that for Fig. 6) was applied (see text). The spectra were fitted with a central Gaussian representing FMT fission, and symmetric pairs of Gaussians representing transfer-fission. Determination of the width of the FMT fission Gaussian was necessary to obtain absolute cross sections of FMT fission (see text).

C. FMT Gaussian σ

Since the procedures developed for extraction of the FMT fission cross sections are sensitive to the widths of the extracted FMT fission component, their systematic behavior is discussed.

The extracted standard deviations (σ) of the Gaussian fits to the FMT peaks in both $[v_{\parallel} - v_{\text{CN}}]$ and v_{\perp} are presented in Fig. 8. These are for the three reactions $^{16}\text{O} + ^{244}\text{Pu}$, $^{12}\text{C} + ^{248}\text{Cm}$ and $^9\text{Be} + ^{249}\text{Cf}$ at approximately matching excitation energies, for the angular range of 95° – 105° , as shown in Figs. 6 and 7. The values show an increasing trend with excitation energy, as would be expected from the increasing number of evaporated neutrons. Moreover, both σ_{\parallel} and σ_{\perp} values lie in close proximity, and are consistent for the three reactions forming similar compound nuclei. This gives confidence in the reliability of the analysis.

D. Determination of absolute cross sections

The solid angle relationships between the forward angle elastic monitor detectors and the MWPC detectors were obtained from simultaneous measurements in both monitor and MWPC detectors of elastic scattering of a heavy beam (^{58}Ni or ^{60}Ni) from a ^{197}Au target at a far subbarrier energy, where Rutherford scattering is expected at all angles. The ^{12}C experiment was normalized using scattering of 126 MeV ^{58}Ni from ^{197}Au , while the ^{16}O and ^9Be experiments used

136.8 MeV ^{60}Ni scattering from ^{197}Au . From the elastic calibration measurement, the ratio of elastic counts detected in the two monitor detectors, and those detected within defined angular ranges of the MWPCs gives information on relative solid angles. Then using the monitor elastic counts from each of the ^9Be , ^{12}C and ^{16}O measurements, the differential cross sections for fissions as a function of angle could be determined. These could be obtained both for all fissions, and for the FMT fission yield determined by gating and subtraction of the transfer-fission component, as described above. To obtain fission cross sections integrated over all angles, the angular distributions must be fitted to allow extrapolation to those angles not covered by the MWPC detectors, namely, close to the beam direction.

E. FMT fission angular distributions

The measured angular distributions for FMT fission for the $^9\text{Be} + ^{249}\text{Cf}$, $^{12}\text{C} + ^{248}\text{Cm}$, and $^{16}\text{O} + ^{244}\text{Pu}$ reactions are shown in Fig. 9, with the corresponding $E_{\text{c.m.}}$ energies given beside the data points. From the extracted fission cross sections as a function of angle, both the total fission cross sections and the angular anisotropies can be determined. The fission fragment angular anisotropy is defined as the ratio of the yield at 180° (or 0°) to that at 90° in the center-of-mass frame.

Theoretical angular anisotropies (A) can be obtained from the statistical saddle point model (SSPM) [11] also referred to

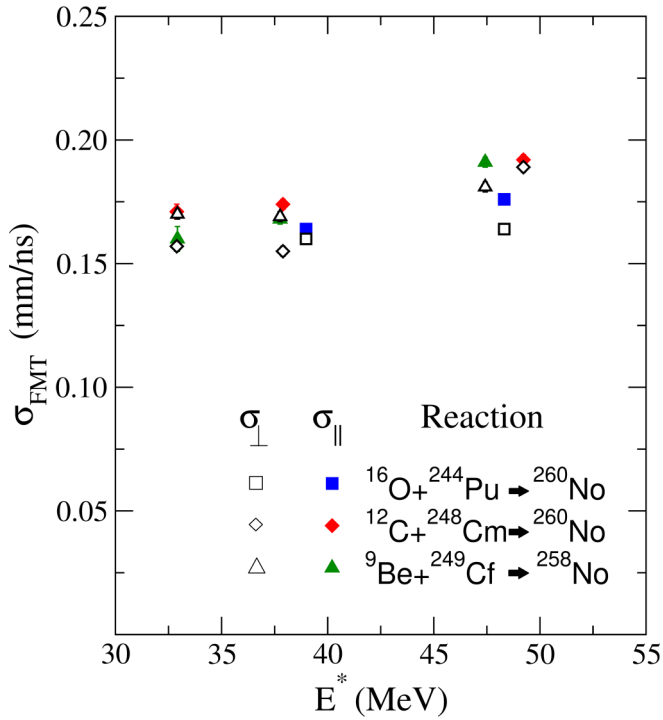


FIG. 8. From the fits to the data shown in Figs. 6 and 7, the best-fitting FMT fission Gaussian standard deviations σ are shown as a function of excitation energy E^* . Both the parallel and perpendicular velocity components, and the data for the different reactions are very similar at the same E^* . The increase with E^* is expected.

as the TSM. An approximate expression for the anisotropy is

$$A \approx 1 + \frac{\langle J^2 \rangle}{4K_0^2}. \quad (4)$$

Within the model, K_0 is given by

$$K_0^2 = \frac{\mathcal{I}_{\text{eff}}}{\hbar^2} T_{\text{sad}}. \quad (5)$$

Here \mathcal{I}_{eff} is the effective moment of inertia at the saddle point and T is the saddle point temperature. The effective moment of inertia is defined in terms of the moments of inertia of the fission saddle-point shape parallel and perpendicular to the fission elongation axis:

$$\frac{1}{\mathcal{I}_{\text{eff}}} = \frac{1}{\mathcal{I}_{\parallel}} - \frac{1}{\mathcal{I}_{\perp}}. \quad (6)$$

For heavy fissile nuclei, the liquid drop model saddle point is relatively compact, therefore \mathcal{I}_{\parallel} and \mathcal{I}_{\perp} are not very different, and \mathcal{I}_{eff} is thus large. This leads to a large value of K_0 and therefore to SSPM calculated anisotropies [see Eq. (4)] that are relatively small. Thus, the anisotropy is expected to be a sensitive measure of whether the system reached the ground-state equilibrium shape. Experimental anisotropies are often larger than those from fusion-fission calculations [1,2,10,16], which is taken to be evidence of quasifission.

Since anisotropies thus need not follow TSM predictions, to fit experimental angular distributions an empirical procedure is generally followed that is not reliant on the TSM calculation of K_0 . Instead K_0 is taken as a free parameter. This procedure was followed, and the best fits to the experimental

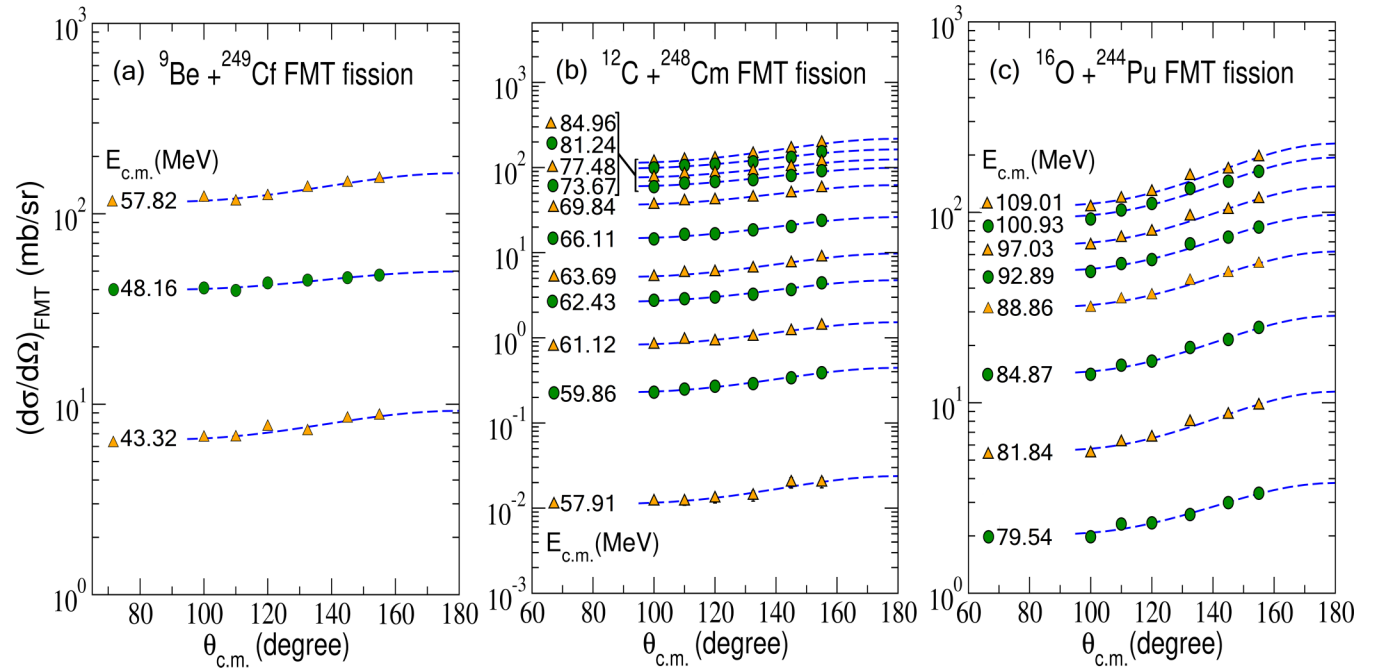


FIG. 9. Deduced FMT fission differential cross sections as a function of angle in the backward hemisphere are shown for the $^9\text{Be} + ^{249}\text{Cf}$, $^{12}\text{C} + ^{248}\text{Cm}$, and $^{16}\text{O} + ^{244}\text{Pu}$ reactions, at the indicated c.m. energies. Almost all experimental uncertainties are smaller than the size of the points. The left-most symbol is for identification of the data, and is not a measured data point. Fits to the distributions using the transition state model formalism, shown by the dashed lines, were used to determine cross sections and angular anisotropies.

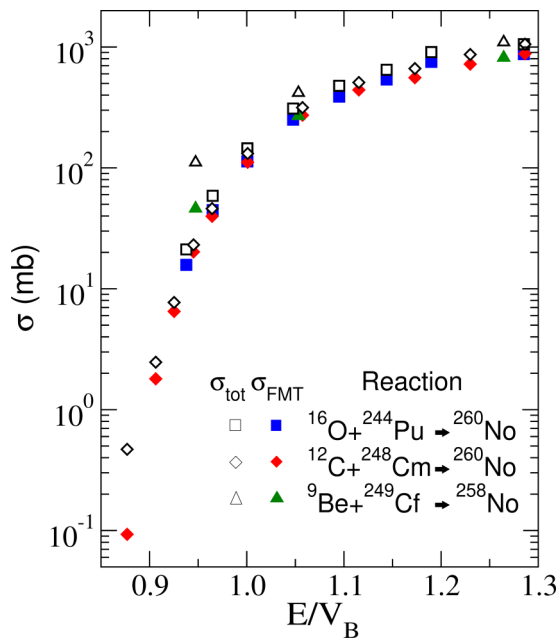


FIG. 10. Total and FMT fission cross sections of ${}^9\text{Be} + {}^{249}\text{Cf}$, ${}^{12}\text{C} + {}^{248}\text{Cm}$, and ${}^{16}\text{O} + {}^{244}\text{Pu}$ reactions as a function of energy with respect to the calculated capture (fusion) barriers. The V_B were calculated using the prescription of Ref. [25], and are given in Table I.

angular distributions were obtained, shown by the blue dashed lines in the Fig. 9.

The FMT fission cross sections and anisotropies have been determined from these fits. Through fitting the angular distributions of all fission events, including transfer fission, total fission cross sections were also determined. The fission cross sections are presented in Sec. III F below. Following the discussion of the measured mass-angle distributions in Sec. III G, presentation and interpretation of the angular anisotropies for FMT fission is given in Sec. III H.

F. Fission cross sections

The cross sections for total fission (σ_{tot}) and FMT fission (σ_{FMT}) for the reactions ${}^9\text{Be} + {}^{249}\text{Cf}$, ${}^{12}\text{C} + {}^{248}\text{Cm}$, and ${}^{16}\text{O} + {}^{244}\text{Pu}$ are presented in Fig. 10, as a function E/V_B , the the ratio of the beam energy in the center of the actinide target material to the calculated capture barrier energy, which is given in Table I.

The cross sections for the other ${}^9\text{Be}$ induced reactions, also as a function of E/V_B , are shown in Fig. 11. A coupled channel (CCFULL [27]) calculation of the capture cross sections for ${}^9\text{Be} + {}^{238}\text{U}$ is also shown in Fig. 11 by the dashed red line. The overall normalization of the ${}^9\text{Be} + {}^{244}\text{Pu}$ cross sections had larger uncertainty than the other targets because the elastic peak in the monitor detectors from the Pu suffered interference from elastic scattering from other elements in the target as a result of degradation of the energy resolution of the monitor detectors.

The cross sections for total fission and FMT fission for all reactions are given in Table III.

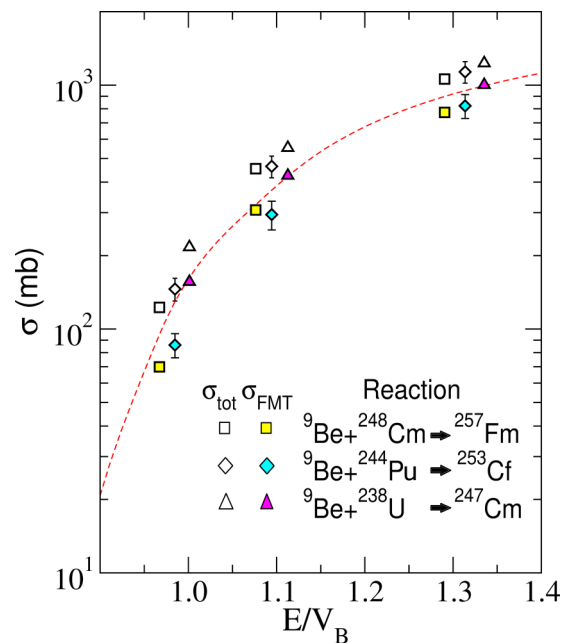


FIG. 11. As in Fig. 10 for the indicated ${}^9\text{Be}$ -induced reactions. The dashed line shows a coupled channels calculation (see text) for ${}^9\text{Be} + {}^{238}\text{U}$. The V_B are given in Table I.

G. FMT mass-angle distributions: No evidence for fast quasifission

Because FMT fission and transfer-fission cannot be fully separated event-by-event, mass-angle distributions (MADs) representing the FMT fission component were obtained by applying a small circular gate of radius 0.30 mm/ns to the fission source velocity distribution over the whole angular range (such as presented in Fig. 14), rather than for the angular range $95^\circ < \theta_{\text{c.m.}} < 105^\circ$ shown in Fig. 4.

Figure 12 shows the FMT MADs for the three reactions ${}^{16}\text{O} + {}^{244}\text{Pu}$, ${}^{12}\text{C} + {}^{248}\text{Cm}$, and ${}^9\text{Be} + {}^{249}\text{Cf}$ at the same beam energies shown previously, having approximately matching E/V_B . Since the circular gate applied in ($[v_{\parallel} - v_{\text{CN}}]$, v_{\perp}) to select FMT fission events has a radius of approximately $2\sigma_{\parallel} \approx 2\sigma_{\perp}$, the cross sections in the MAD plots represent $\approx 60\%$ of the total FMT fission yields. The MADs for the Pb targets are shown in the right-hand panels. Since fusion-fission is expected for those reactions, it is no surprise that they show no mass-angle correlation.

None of the MADs for the actinide target reactions show any discernible mass-angle correlation, within experimental uncertainty. Thus, no significant fast mass-asymmetric quasi-fission component is present. This is not unexpected, but evidence for slow quasifission is seen for all reactions, as discussed below.

H. FMT fission angular anisotropies: Evidence for slow quasifission

Measured fission fragment angular anisotropies (A) of all the reactions under investigation are shown as a function of E/V_B in Fig. 13. The results at energies well above-barrier ($E/V_B \approx 1.25$) are discussed first.

TABLE III. Measured total and FMT fission cross-sections for all the reactions studied in this work, as a function of the center of mass energy ($E_{c.m.}$) at the center of the actinide layer of the target. Quoted uncertainties principally arise from statistical errors propagated through the fitting of the angular distributions, however for ${}^9\text{Be} + {}^{244}\text{Pu}$, significant uncertainties arise from determination of the monitor elastic counts (see text).

Reactions	$E_{c.m.}$ (MeV)	E^* (MeV)	σ_{tot} (mb)	σ_{FMT} (mb)
${}^{16}\text{O} + {}^{244}\text{Pu}$	79.54	39.00	21.2 ± 0.2	15.8 ± 0.2
	81.84	41.30	58.8 ± 0.5	44.7 ± 0.5
	84.87	44.33	145.1 ± 0.9	113.2 ± 0.9
	88.86	48.32	309.8 ± 1.8	250.7 ± 1.7
	92.89	52.35	477.8 ± 2.4	388.6 ± 2.4
	97.03	56.49	648.6 ± 2.4	538.6 ± 2.4
	100.93	60.39	907.6 ± 2.2	754.0 ± 2.2
	109.01	68.47	1055 ± 5	874 ± 5
	${}^{12}\text{C} + {}^{248}\text{Cm}$	57.91	29.70	0.47 ± 0.01
59.86		31.64	2.47 ± 0.03	1.80 ± 0.02
61.12		32.90	7.71 ± 0.10	6.50 ± 0.10
62.43		34.21	23.08 ± 0.20	20.20 ± 0.20
63.69		35.47	46.0 ± 0.4	39.8 ± 0.4
66.11		37.89	131.5 ± 1.0	111.4 ± 1.0
69.84		41.62	315.6 ± 2.4	272.6 ± 2.4
73.67		45.45	509 ± 3	442 ± 3
77.48		49.26	663 ± 4	557 ± 4
81.24		53.02	868 ± 5	722 ± 5
84.96		56.74	1055 ± 5	881 ± 5
${}^9\text{Be} + {}^{249}\text{Cf}$	43.32	32.92	111.1 ± 0.6	46.1 ± 0.4
	48.16	37.76	418 ± 3	269.2 ± 2.3
	57.82	47.42	1096 ± 7	817 ± 7
${}^9\text{Be} + {}^{248}\text{Cm}$	43.36	33.51	122.6 ± 0.7	69.9 ± 0.5
	48.25	38.40	454.2 ± 2.5	307.6 ± 2.2
	57.85	48.00	1059 ± 6	773 ± 6
${}^9\text{Be} + {}^{244}\text{Pu}$	43.36	35.21	146 ± 16	86 ± 10
	48.19	40.04	464 ± 47	294 ± 40
	57.84	49.69	1133 ± 114	822 ± 92
${}^9\text{Be} + {}^{238}\text{U}$	43.33	36.45	216.7 ± 1.0	156 ± 0.9
	48.16	41.28	553 ± 3	426 ± 3
	57.79	50.91	1230 ± 7	1002 ± 7

The anisotropies increase significantly with projectile mass, which is expected, since Eq. (4) shows that (A-1) is proportional to $\langle J^2 \rangle$, and this will certainly increase with projectile mass. However, the measured increase is considerably larger than predicted for fusion-fission by TSM calculations, which are indicated by the color-matched lines. The TSM calculations require capture angular momentum distributions (obtained from coupled-channels fits to the experimental capture cross sections presented in Sec. III F), effective moments of inertia and temperatures. For the reactions studied here, the effective moment of inertia (\mathcal{I}_{eff}) as well as the fission barrier height (B_f) and ground-state rotational energy (required to evaluate temperatures) were calculated for the compound nucleus ${}^{254}\text{Fm}$, since the rotating finite range model (RFRM) calculations [28] give reliable values only for nuclei with $20 \leq Z \leq 100$.

The observation of increased anisotropies for fission events peaked at mass-symmetric splits has been previously identified with the presence of slow quasifission [1,2,16]. The current anisotropy values are consistent with previous measurements [2] for reactions with lighter actinide nuclei. Unlike the ${}^{12}\text{C}$ and ${}^{16}\text{O}$ reactions, the experimental anisotropies for the ${}^9\text{Be} + {}^{249}\text{Cf}$, ${}^{248}\text{Cm}$, ${}^{244}\text{Pu}$, and ${}^{238}\text{U}$ reactions at $E/V_B \gg 1$ are close to the predictions for fusion-fission. This is consistent with a reduced or zero contribution from quasifission, which might be expected given the lower mass and charge of ${}^9\text{Be}$. Significantly, the similarity between TSM calculations and experiment supports the validity of the TSM approach to calculating fission anisotropies, even for these very heavy compound nuclei. This gives quantitative support to the interpretation of anisotropies exceeding TSM calculations as being the result of a component of quasifission.

Now we consider the dependence of anisotropies on beam energy. For reactions of ${}^{12}\text{C}$ and ${}^{16}\text{O}$ with actinide nuclei, it has long been established [2,16,29] that as the beam energy falls, anisotropies initially fall approaching the barrier (though remaining well above TSM calculations), then rise to significantly higher values at subbarrier energies. This has been explained phenomenologically as being due to the transition from predominantly axial collisions at subbarrier energies to predominantly equatorial collisions at above barrier energies [15,16,29], with the axial (tip) collisions favoring quasifission. The observed trends in anisotropies are in agreement with the systematics of Ref. [2].

New information comes from the measurements for ${}^9\text{Be} + {}^{249}\text{Cf}$, ${}^{248}\text{Cm}$, ${}^{244}\text{Pu}$, and ${}^{238}\text{U}$. They show a small but consistent increase as $E_{c.m.}/V_B$ falls below 1.0, mirroring the behavior of the ${}^{12}\text{C}$ and ${}^{16}\text{O}$ reactions. If the interpretation for the ${}^{12}\text{C}$ and ${}^{16}\text{O}$ induced reactions is correct, this suggests that even for a projectile as light as ${}^9\text{Be}$, a small fraction of capture reactions with the tips of the deformed actinide nuclei (increasingly dominant at subbarrier energies) does not result in fusion, but instead result in slow quasifission.

Comparison of measured mass distributions might offer another avenue to investigate the significance and characteristics of quasifission in these reactions.

I. FMT mass-ratio spectra: Differences between projectiles

Comparison of the mass-ratio spectra between the different reactions at the same excitation energy could be valuable in providing additional evidence for the presence of quasifission, independent of the angular distributions. Possible signatures of quasifission are considered below.

1. Expected differences between fusion-fission and quasifission mass distributions

Liquid drop model calculations of the height of the fission barrier as a function of mass asymmetry (and also of the potential energy at elongations greater than the fission barrier) show an essentially parabolic distribution with a minimum at mass symmetry. This results in the expectation of mass distributions of Gaussian form, peaked at symmetric mass-splits. This condition is expected to be realized for fusion-fission at high excitation energies where structure in the potential

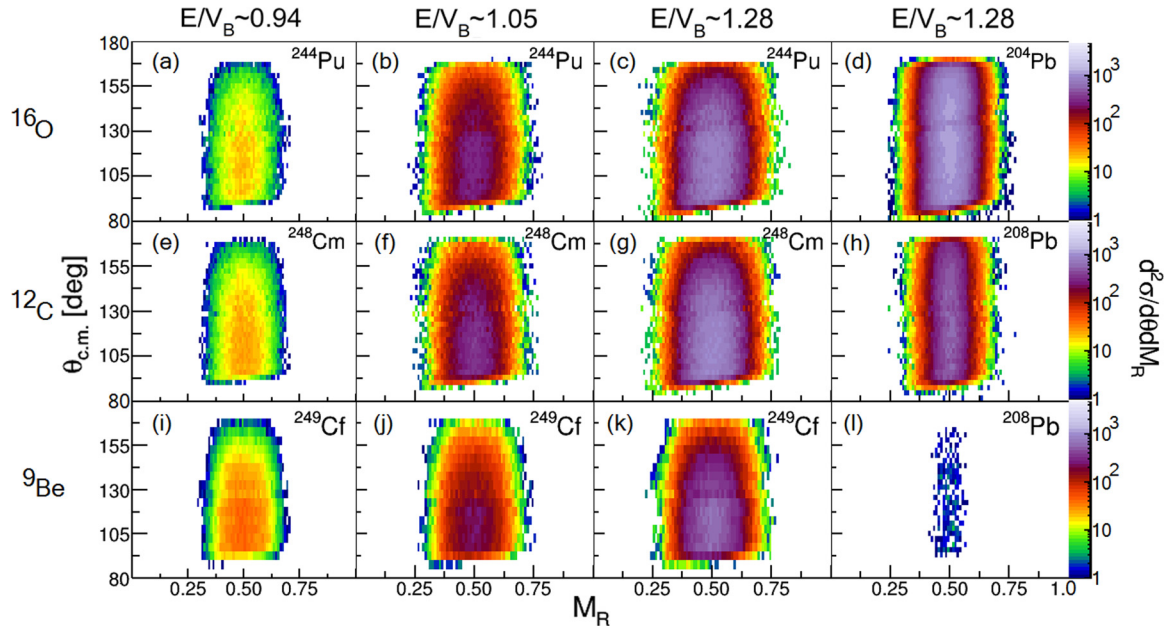


FIG. 12. Experimental FMT mass-angle distributions (MADs) for the same reactions as in Fig. 4, for approximately matching E/V_B as indicated. MAD for $^{16}\text{O} + ^{244}\text{Pu}$, ^{204}Pb are in the top row, $^{12}\text{C} + ^{248}\text{Cm}$, ^{208}Pb in the middle row, and $^9\text{Be} + ^{249}\text{Cf}$, ^{208}Pb in the bottom row. As for the reactions with the Pb targets, no mass-angle correlation is seen within experimental accuracy for the reactions with the actinide targets, indicating the absence of fast quasifission in all cases.

energy due to shells in the nascent fragments is fully washed out.

In the case of fast quasifission, the centroid (and perhaps the width) of the mass distribution varies with angle, and is

not centered at mass symmetry except at $\theta_{c.m.} = 90^\circ$. The mass distribution integrated over all angles would be expected to be wide, since the system separates at a range of times before mass-equilibrium is reached, thus having a memory of the projectile-target mass-asymmetry.

For slow quasifission, without a mass-angle correlation (as in the present reactions), the mass-asymmetry degree of freedom is expected to be close to equilibrated. Thus, in the absence of shell effects, a Gaussian distribution should also be expected, but if full equilibrium in mass asymmetry was not achieved, the width should be greater than for fusion-fission. Even if the mass-asymmetry were fully equilibrated in the same way as it is fusion-fission, the mass width should still be greater, as explained below, because quasifission (essentially by definition) is faster than fusion-fission. The time is expected to be shorter since the path in deformation space from contact to scission is shorter in the case of quasifission, bypassing the compact equilibrium configuration.

At the low excitation energies of this work, it is unlikely that neutron emission would be significant before quasifission (including slow quasifission) occurs. This suggests that slow quasifission dynamics occurs here without any loss of energy due to neutron evaporation, and therefore occurs at the initial excitation energy of the system, in a similar way to first-chance fission. In contrast, for fusion-fission it is known that multichance fission is significant [8,30–34]. This means that fusion-fission also occurs after emission of one or more neutrons, and this can be a major contributor to the total FMT fission yield. Thus, the mean excitation energy above the potential energy surface should be higher in quasifission than in fusion-fission. Due to increased thermal fluctuations, a higher excitation energy results in an increased mass width.

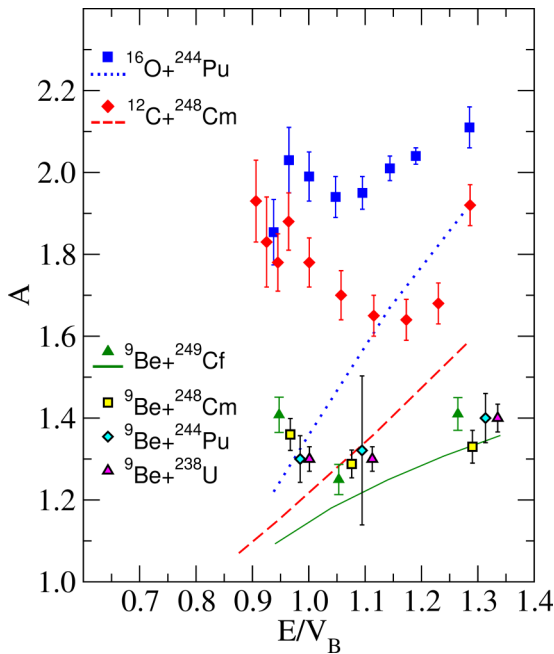


FIG. 13. FMT fission angular anisotropies (A) plotted as a function of E/V_B for the reactions forming $^{258,260}\text{No}$. The dotted, dashed and full lines represent TSM calculations of fusion-fission anisotropies of $^{16}\text{O} + ^{244}\text{Pu}$, $^{12}\text{C} + ^{248}\text{Cm}$, and $^9\text{Be} + ^{249}\text{Cf}$, respectively.

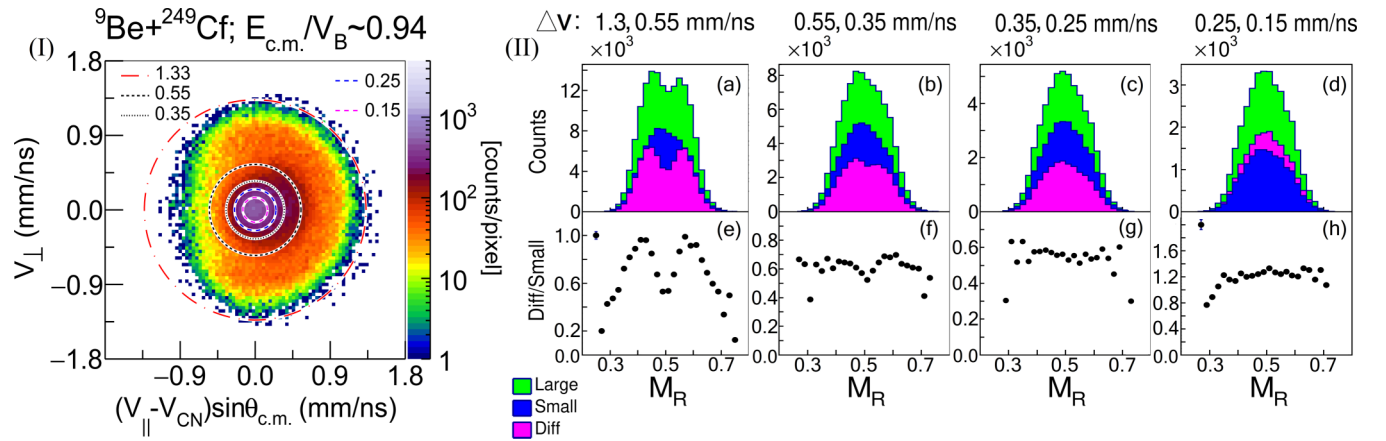


FIG. 14. Panel (I) shows the fission source velocity distribution for the lowest energy ${}^9\text{Be} + {}^{249}\text{Cf}$ measurement, where the ratio of transfer fission to FMT fission is the largest. The data are for the full range of angles. Successively smaller circular cuts of radius ΔV have been applied. The largest ($\Delta V = 1.3$ mm/ns) includes all FMT and transfer fission, while the smallest ($\Delta V = 0.15$ mm/ns) is similar to the standard deviation of the FMT fission distribution. The mass-ratio spectra associated with successively smaller circular cuts ΔV are presented in Panel (II) (a) to (d) as labeled, showing the spectra inside the largest circle (green shaded, labeled **Large**), those inside the smaller circle (blue shaded, labeled **Small**), and the differences (magenta shaded, labeled **Diff**). The ratios of the difference mass spectra (in the outer annulus) in magenta to those of the inner circle (in blue) are shown below in (e)–(h) as a function of mass-ratio. For the smaller cuts, the ratio is independent of mass in the region of significant fission yield, indicating that these spectra are essentially not influenced by the transfer-fission, and thus correctly represent the FMT fission mass spectrum.

Langevin transport model calculations [9] have indicated one possible origin of slow quasifission events. The shape evolution of many trajectories, from a starting point representing the contact configuration, is followed over a calculated potential energy surface. Trajectories that never reach the compact equilibrium pocket, but have passed inside the fission saddle point, have been termed “deep quasifission.” These events pass over the true fission saddle-point in “making their escape,” in the same way as fusion-fission, but on a more rapid time scale. This process may well make a major contribution to the class of quasifission events experimentally characterized [1,2] as “slow quasifission.”

As noted, at the same excitation energy and angular momentum, the higher excitation energy for slow quasifission compared with the mean for (multichance) fusion-fission will result in a somewhat wider mass distribution. However, a more sensitive measure may well be the attenuation with E^* of features in the mass spectrum resulting from shell effects. Because of the rapid attenuation of shell effects with excitation energy [35], shell-dependent structure in the mass-distributions should be reduced in quasifission compared with fusion-fission occurring from the same *initial* excitation energy [8]. This approach can be used if the fission mass distributions show evidence for the influence of shell effects.

The optimal selection of FMT events will be discussed below, then the spontaneous fission characteristics of relevant No isotopes will be reviewed, before the presentation and interpretation of the experimental FMT fission mass spectra.

2. Minimizing the influence of transfer-fission

It is necessary to reject as far as possible fission events following transfer reactions, which result in lighter fissioning nuclei produced at lower excitation energies than in fusion-

fission. As noted previously, because of the overlap of the source velocity distributions of FMT fission and transfer fission, in principle it is not possible to reject *every* transfer-fission event. However, as seen in Fig. 4, for the ${}^{12}\text{C}$ and ${}^{16}\text{O}$ measurements, the overlap between FMT fission and transfer-fission is small, and by gating on the central FMT fission group the contribution of transfer-fission is negligible. However, for the ${}^9\text{Be}$ reactions, there is significant overlap.

To minimize the fraction of “contaminant” events coming from transfer-fission, in principle the smaller the gate around (0, 0) in the fission source velocity distribution, the better. However, this also cuts down the statistics, and thus the precision of the mass-ratio spectra. To determine the optimum cut, a procedure was developed that is illustrated in Fig. 14, and described below. The figure shows data for all angles at the lowest ${}^9\text{Be} + {}^{249}\text{Cf}$ energy, where the fraction of transfer-fission is largest. This is thus the most severe test of the method.

Mass-ratio spectra have been determined for different gates on the fission source velocity distribution, consisting of circles centered on (0,0) with decreasing radii ΔV ; the gates are illustrated in Fig. 14, Panel (I). The fraction of transfer-fission in the experimental spectra is expected to decrease with gates of smaller and smaller radii. The largest gate with $\Delta V = 1.3$ mm/ns includes all FMT and transfer fission events. The smallest, with $\Delta V = 0.15$ mm/ns is slightly smaller than the standard deviation of the FMT fission events. The mass-ratio spectra associated with successively smaller circular cuts are presented in the upper panels of Fig. 14, Panel (II), from left to right, showing the spectra inside the largest circle (green shaded, labeled **Large**), those inside the smaller circle (blue shaded, labeled **Small**), and the spectra corresponding to the annular region between the two circular gates (magenta shaded, labeled **Diff**).

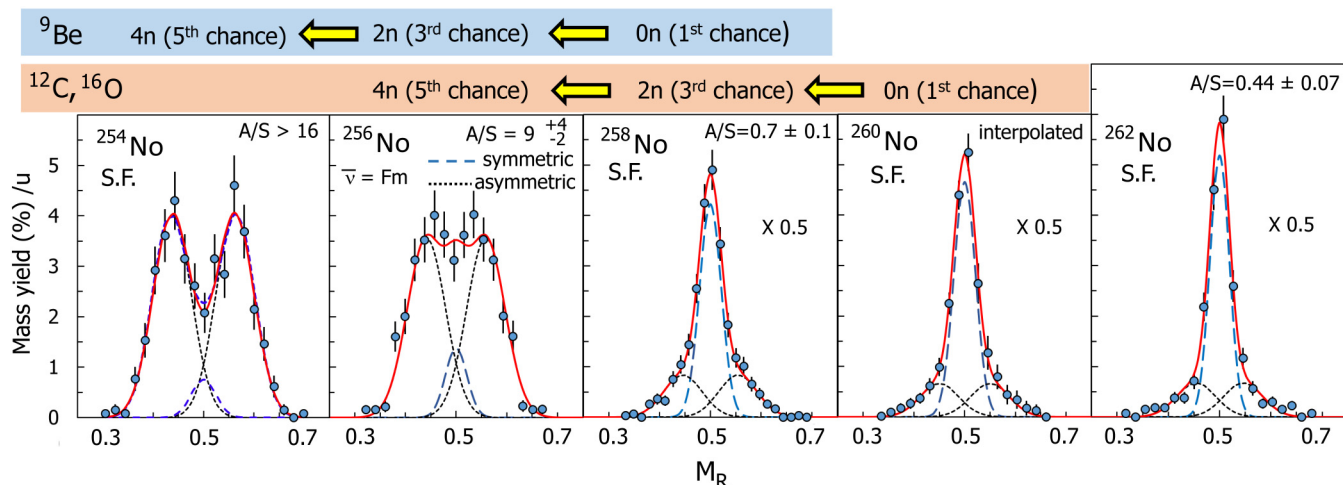


FIG. 15. Spontaneous fission mass-ratio distributions for the indicated No isotopes [36–38]. These are populated in multichance fission in the reactions studied here, as indicated above the spectra. In the absence of a measurement for ^{260}No , an interpolation between ^{258}No and ^{262}No was taken. The y axis represents probability per mass unit, normalized to 200%. The probabilities for $^{258-262}\text{No}$ are scaled by 0.5. The data have been fitted with a mass-asymmetric and mass-symmetric component. The former width and mass centroids were fixed based on the values from the fit to the ^{254}No distribution: the mean mass of the heavy fragment was then fixed at 143 for all isotopes. The width of the mass-symmetric component for the $^{254,256}\text{No}$ fits was fixed from that from the ^{258}No spectrum. The value of A/S given for each measured spectrum is the ratio of asymmetric to symmetric yield from the fits.

The ratios of the mass spectra in the outer annulus (magenta) to those of the inner circle (blue) are shown below as a function of mass-ratio. For the cuts corresponding to the larger radii, the ratio spectra show a double-peaked structure resulting from the dominant mass-asymmetric fission of actinide nuclei at the lower excitation energies populated following transfer reactions. For the smaller cuts, the ratio is independent of mass in the region of significant fission yield, indicating that these spectra are essentially not influenced by transfer-fission, and thus are correct representations of the FMT fission mass-ratio spectrum.

From this analysis for the lowest energy $^9\text{Be} + ^{249}\text{Cf}$ measurement, the FMT fission gate radius to determine the FMT fission mass-ratio spectra was chosen to be 0.30 mm/ns. For consistency, and to minimize the contribution from transfer-fission, the same limit was applied for the higher $^9\text{Be} + ^{249}\text{Cf}$ energies, and for all $^{12}\text{C} + ^{248}\text{Cm}$ and $^{16}\text{O} + ^{244}\text{Pu}$ measurements.

3. Spontaneous fission mass distributions for No isotopes

The effect of quantum shells on the mass distributions of No isotopes is expected to be the most pronounced at the lowest excitation energy. Fission from the ground-state, i.e., spontaneous fission (SF), is thus the ideal probe of the shell effects that might influence the mass distributions at the higher excitation energies relevant to the reactions investigated here.

Spontaneous fission mass-ratio distributions (post-neutron emission) have been determined from coincident measurements [36–38] of the energies of the two fission fragments for the isotopes $^{252,254,256,258,262}\text{No}$. These have been converted into scission mass distributions through assumptions about the mass dependence of the post-scission neutron multiplicities [37]. We are not aware of any SF measurement for

^{260}No , the compound nucleus formed in the $^{12}\text{C} + ^{248}\text{Cm}$ and $^{16}\text{O} + ^{244}\text{Pu}$ reactions. However, the mass distributions measured for ^{258}No and ^{262}No are not very different, so the distribution for ^{260}No has been estimated by averaging those for ^{258}No and ^{262}No .

The derived spontaneous fission mass-ratio distributions for $^{254,256,258,260,262}\text{No}$ are shown in Fig 15. There is a dramatic change with neutron number, with the lightest showing mass-asymmetric fission consistent with the Standard II mode [39], while the heaviest is dominated by a narrow mass-symmetric split, seemingly with a high TKE component [36] as found in ^{258}Fm and heavier neighbors. This is believed to be associated with the mass-symmetric fragments being sufficiently close to the ^{132}Sn doubly magic spherical nucleus.

There might be a component of mass-asymmetric fission for all the presented isotopes. To test this quantitatively, the mass-ratio spectra have been fitted with a mass-asymmetric and mass-symmetric mode. The former was parameterized as two Gaussians, symmetrically deviating from $M_R = 0.5$. The widths in M_R were fixed to those determined from fitting the ^{254}No data, for which a mass-symmetric mode is not expected. The peak positions were fixed to give the same heavy fragment mass as for ^{254}No , namely, $A = 143$. The width of the single Gaussian centered at $M_R = 0.5$, representing the mass-symmetric component, was determined from fitting the heavier isotopes. The fit to ^{254}No including a symmetric component (dashed blue lines) gave a larger reduced chi-squared than omitting this component, shown by the black dotted lines and red total fit, thus its presence is not supported by the existing data.

The components and total fits are shown in Fig 15, and clearly give a good representation of the data, with an average reduced χ -squared of 0.96. They support a contribution from the mass-asymmetric mode for all isotopes despite the clear

change in the measured dominant fission mode, from mass asymmetric to mass-symmetric as the neutron number of the fissioning nucleus increases. This transition is quantified by the ratio of asymmetric to symmetric yield, denoted A/S , given in Fig 15 for all the measured spectra. Such a transition in multi-mode fission has been obtained from four-dimensional Langevin transport calculations over a two center shell model potential for many nuclei in this mass region [40], including ^{256}No .

The fission observed in this work for the ^9Be reaction, forming ^{258}No , will in principle sample multichance fission of nuclei between ^{258}No and ^{254}No ($4n$ emission), as indicated in the figure. The ^{12}C , ^{16}O reactions, which both form ^{260}No , will have contributions from ^{260}No to ^{256}No . The weighting of each fission chance, from first-chance to last chance, will depend on the absolute probabilities at each chance. Because of the low liquid drop fission barriers of No isotopes, the probabilities will in turn will depend on the damping of shell effects with excitation energy.

If the shell effects were completely damped at the excitation energy for first-chance fission, the low liquid drop fission barrier might be expected to result in first-chance fission being completely dominant, resulting in a mass distribution resulting from the liquid drop model potential (the super-long mode). This would be of Gaussian shape centered at symmetry, but considerably wider than the observed mass-symmetric spontaneous fission mode.

If the shell damping was not complete at the excitation energies relevant to this work, and was *the same* for the mass-asymmetric and mass-symmetric modes, then the spontaneous fission data suggest that the mass distributions for the ^{12}C , ^{16}O reactions should be narrower than those for the ^9Be reaction.

If there were residual effects of quantum shells in the mass distributions, indicating the presence of multichance fission, then this could give information on the presence of quasifission, as was proposed above.

4. Structure in the measured FMT fission mass distributions

The mass-ratio spectra for the three reactions $^9\text{Be} + ^{249}\text{Cf}$ (first column), $^{12}\text{C} + ^{248}\text{Cm}$ (second column), and $^{16}\text{O} + ^{244}\text{Pu}$ (third column), measured at approximately matching excitation energies (averaging 48 MeV, 38 MeV, and 33 MeV) are shown in Figs. 16(a)–16(c), 16(h)–16(j), and 16(r), 16(s) respectively, as indicated.

The first observation is that the mass-ratio spectra for each projectile and excitation energy are very similar, showing a wide distributions peaked at mass-symmetry. The question is, do they show any evidence at all of shell effects?

In the absence of shell effects, the mass ratio spectra would be expected to be well-described by a single Gaussian. Gaussian fits are shown by the black curves: they do not describe the measured spectra very well. The ratios of experiment to the single Gaussian fits are shown below each mass-ratio spectrum in Figs. 16(d)–16(f), 16(k)–16(m), and 16(t), 16(u). The double-peaked structure seen in all cases demonstrates the presence of significant mass-asymmetric fission. Evidence for a narrow mass-symmetric fission mode is not visible. The mass asymmetric structure is expected to be due to shell

effects in the fusion-fission component, or could also be due to shell effects and/or incomplete mass equilibration during the quasifission dynamics.

The mass-ratio spectra were then fitted with a double-Gaussian function, comprising two Gaussians of the same height and width, and with the same absolute offset from mass-symmetry, but of opposite sign. The two components of these fits are shown by the green double dot-dashed lines, and the total fit by the red dashed lines. These give a very good representation of the experimental data, far better than the single Gaussian fits.

The fitted mass-asymmetric peak centroids are consistently at mass-ratios ≈ 0.45 and ≈ 0.55 in all cases, within experimental uncertainty. For first-chance fission these correspond to fragment masses at scission of 116–117 and 142–143. For last-chance fission, at the lowest excitation energies (where the effect of shells is expected to be most significant) masses would be ≈ 115 and ≈ 140 . The fit to the spontaneous fission asymmetric mode for ^{254}No shows peaks at $M_R = 0.437$, 0.563 , corresponding to masses 111 and 143. The heavy fragment mass corresponds closely to that of the Standard II fission mode [39]. This mode, whose origin has recently been suggested to be octupole shell effects [41], plays a very important role in fission mass distributions over a wide range of actinide nuclei.

The similarity in the mass peaks for the different reactions and excitation energies suggests that there is a common origin, and so it is concluded that the shell effects responsible for the Standard II mode are most likely to be responsible for the mass-asymmetry in all cases, rather than quasifission dynamics.

Spontaneous fission of ^{258}No shows a significant narrow mass-symmetric peak, as well as mass-asymmetric shoulders [36]. The presence of such a component can be investigated through the ratios of experiment to the double Gaussian fit, which are shown for $E^* = 38$ MeV in Figs. 16(n), 16(o) and 16(p). There is a consistent small residual structure at mass-symmetry seen in Figs. 16(n), 16(o), and 16(p), hinting at a weak mass-symmetric mode. For the $^9\text{Be} + ^{249}\text{Cf}$ reaction, ^{258}No corresponds to first-chance fission at the highest E^* , while for the other two reactions it corresponds to third-chance fission after emission of two neutrons, and thus a much lower excitation energy. Knowledge of the distribution of fission cross section with excitation energy, and the possibly different damping of the shell effects with excitation energy resulting in the narrow mass-symmetric and wide mass-asymmetric fission modes would be required to interpret this possible weak mass-symmetric peak.

It is concluded that overall, the measured FMT fission mass-ratio spectra obtained in this work show the effects of a predominant mass-asymmetric fission mode, independent of compound nucleus, projectile, and beam energy (excitation energy). This uniformity in mass spectrum is not at all the case for spontaneous fission of No isotopes. This contrast might be explained if the narrow symmetric fission mode was less robust against excitation energy than the mass-asymmetric mode. Further multi-component analysis could be carried out, but this is not the goal of this investigation.

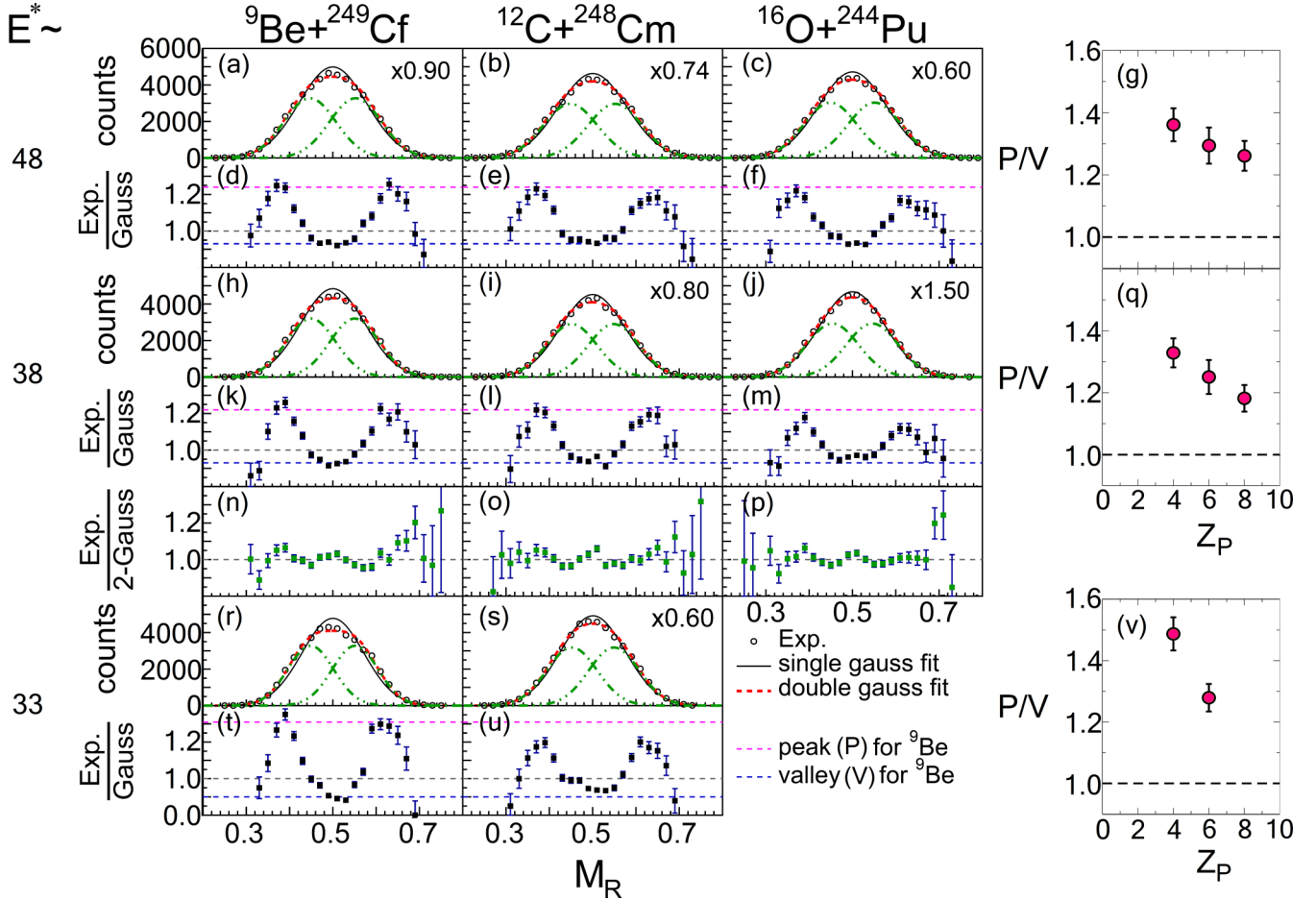


FIG. 16. Analysis of the mass-ratio (M_R) spectra for each reactions (in the columns) and for similar excitation energies (in the rows). Spectra of counts vs. M_R are presented in panels (a)–(c), (h)–(j), and (r), (s) corresponding to excitation energies E^* of ≈ 48 , 38 and 33 MeV, respectively (as indicated on the left). The counts in the spectra are multiplied by the factor given in each panel (if not unity). The thin black curves are the best-fitting single Gaussians. The ratios of the experimental data to the fits are shown below in panels (d)–(f), (k)–(m), and (t), (u). It is concluded that the double-peaked structure is evidence for shell effects. The magenta and blue dashed lines in these panels show the mean peak (P) and valley (V) values for the ${}^9\text{Be}$ reactions. The ${}^{12}\text{C}$ and ${}^{16}\text{O}$ data show peak and valley values closer to unity, attributed to slow quasifission (see text). These results are summarized in the ratios (P/V) as a function of projectile atomic number Z_P shown for each excitation energy in the right-most panels (g), (q), and (v). The M_R spectra in panels (a)–(c), (h)–(j), and (r), (s) are better fitted by two Gaussians, their sum being indicated by the red dashed curves and the individual Gaussians by the green double dot-dashed curves. For $E^* = 38$ MeV, the ratios of experiment to these two-Gaussian fits are shown in panels (n), (o), and (p) (see text).

From the observation of fission mass distributions with structure resulting from shell effects, it follows that the mass spectra should be sensitive to the presence of quasifission, since even slow quasifission should occur before any neutron evaporation, unlike fusion-fission. Quasifission is therefore expected to occur at a higher excitation energy, equivalent to that for first-chance fusion-fission. Shell effects in the mass spectra should be more attenuated for (first-chance) quasifission than for (multichance) fusion-fission. The presence of quasifission would be expected to attenuate structure in the mass distributions resulting from shell effects in the nascent fragments.

5. Evidence for slow quasifission from mass-ratio spectra

Since the parameters of the double Gaussian fits are unconstrained by theory or systematics, the simplest way to

quantify the influence of the shell effects is by the ratio of the experimental data to the single Gaussian fit.

The ratios of the experimental M_R spectra to the single Gaussian fits shown in Figs. 16(d)–16(f), 16(k)–16(m), and 16(t), 16(u) were characterized by their peak (mass-asymmetric) value, and the value characteristic of the valley (at mass-symmetry, between the peaks). These two values for the ${}^9\text{Be} + {}^{249}\text{Cf}$ measurements (the reaction expected to have the smallest fraction of quasifission) are indicated in the panels by the magenta and blue dashed lines respectively labeled peak (P) and valley (V). The lines are extended to the ${}^{12}\text{C}$ and ${}^{16}\text{O}$ panels at the same E^* to enable a clear comparison between the reactions. It is clear that in all cases this ratio at the peaks is lower and generally at the valley is higher for the ${}^{12}\text{C}$ and ${}^{16}\text{O}$ reactions. This is consistent with a reduced influence of shell effects, as expected at higher excitation energy, and thus a larger

fraction of slow quasifission, as discussed in more detail below.

For each excitation energy, the peak to valley ratios for the three reactions are shown as a function of projectile atomic number Z_P in the right-most Figs. 16(g), 16(q), and 16(v).

At $E^* = 33$ MeV, both the ${}^9\text{Be}$ and ${}^{12}\text{C}$ reactions are below-barrier (see Fig. 2), where the quasifission probability for each reaction is expected to be at its largest, due to the dominance of capture reactions with the tips of the deformed target nuclei. The angular anisotropies are much larger for ${}^{12}\text{C}$ than for ${}^9\text{Be}$ (see Fig. 13), generally interpreted as showing a higher probability of slow quasifission [2]. Looking at the structure in the mass-ratio spectra, as seen in Exp./Gauss plots in Figs. 16(d)–16(f), 16(k)–16(m), and 16(t)–16(u), as well as in terms of peak to valley ratio (P/V) shown in Figs. 16(g), 16(q), and 16(v), the structure is much weaker for ${}^{12}\text{C}$ than for ${}^9\text{Be}$, despite the initial excitation energies being the same. This would occur if the fission mass-split were determined at a higher average excitation energy for the ${}^{12}\text{C}$ reaction. This will be the result if there is a higher probability of quasifission in the ${}^{12}\text{C}$ reaction compared with ${}^9\text{Be}$.

Thus, comparing the ${}^9\text{Be}$ and ${}^{12}\text{C}$ fission characteristics at subbarrier energies in both reactions, at $E^* = 33$ MeV, the two independent observables of the angular distribution and the mass-distribution consistently indicate the presence of increased quasifission in the ${}^{12}\text{C} + {}^{248}\text{Cm}$ reaction.

At $E^* = 38$ MeV, data were obtained for all three reactions. The ${}^9\text{Be} + {}^{249}\text{Cf}$ reaction is above-barrier, ${}^{12}\text{C} + {}^{248}\text{Cm}$ at the barrier, and ${}^{16}\text{O} + {}^{244}\text{Pu}$ below-barrier. Based on both the projectile mass (or charge), and the collision energy, the probability of quasifission would be expected to be lowest for ${}^9\text{Be}$, and highest for ${}^{16}\text{O}$. The deviation of the angular anisotropies from TSM expectations for fusion-fission (seen clearly in Fig. 13) are consistent with this expectation. Turning to evidence in the mass spectra, the P/V values for this energy, plotted in Fig. 16(q), are consistent too, showing a decrease in P/V as a function of Z_P (recall that lower P/V values signify a higher average excitation energy, and thus a higher probability of quasifission).

At $E^* = 48$ MeV all reactions are above-barrier, thus the quasifission probability is expected to be smaller than at the lower E^* . Consistent with this, the P/V values show a weaker dependence on Z_P .

The comparison of mass-ratio spectra between the two reactions ${}^{12}\text{C} + {}^{248}\text{Cm}$ and ${}^{16}\text{O} + {}^{244}\text{Pu}$, both forming ${}^{260}\text{No}$ at the same excitation energy, consistently shows the effects of shell structure to be weaker in the second reaction, where the fission anisotropy data suggest [2] a higher probability of quasifission. The trend continues for the ${}^9\text{Be} + {}^{249}\text{Cf}$ reaction, but since this forms ${}^{258}\text{No}$, firm conclusions require more assumptions.

Before completing this analysis, the possible consequence of the observed narrow mass-symmetric fission mode in spontaneous fission of ${}^{258}\text{No}$ should be discussed. If this dominant spontaneous fission mode of ${}^{258}\text{No}$ (and very likely [38] also of ${}^{259,260}\text{No}$) persisted at the relevant excitation energies for the reactions forming ${}^{260}\text{No}$, this would make the interpretation more complex, since this component should be much weaker for the ${}^9\text{Be} + {}^{249}\text{Cf}$ reaction forming the compound

nucleus ${}^{258}\text{No}$. However, the very weak contribution of this mode inferred from the spectra measured for the ${}^{12}\text{C}$ and ${}^{16}\text{O}$ reactions forming ${}^{260}\text{No}$ would constitute even stronger evidence for a major component of quasifission in these reactions. If the proportion of quasifission were determined for these reactions, the argument could be inverted, and information on the damping of this mode with excitation energy might be obtained.

In this work, for the first time consistent evidence of slow quasifission in *both* the fission angular anisotropies and the fission mass distributions has been obtained in reactions on actinide targets. The proportion of slow quasifission compared to fusion-fission appears to vary systematically with the projectile charge (mass), increasing from ${}^9\text{Be}$ through ${}^{12}\text{C}$ to ${}^{16}\text{O}$. The evidence for quasifission is strongest at energies below the capture barrier, consistent with previous work, attributed to capture reactions with the tips of the deformed target nuclei.

IV. DISCUSSION AND SUMMARY

Fission fragment mass and angle distributions were measured for the reactions ${}^{16}\text{O} + {}^{244}\text{Pu}$ and ${}^{12}\text{C} + {}^{248}\text{Cm}$ (both forming ${}^{260}\text{No}$) and ${}^9\text{Be} + {}^{249}\text{Cf}$ (forming ${}^{258}\text{No}$) to investigate evidence for the presence of quasifission. Measurements were also carried out (at the same beam energies) of fission for the reactions ${}^9\text{Be} + {}^{238}\text{U}$, ${}^{244}\text{Pu}$, and ${}^{248}\text{Cm}$.

In such reactions with actinide target nuclei, the contributions of fission following transfer reactions can be very significant, particularly for reactions with ${}^9\text{Be}$. This must be minimized to allow accurate determination of characteristics of fission following capture of the full projectile mass, referred to as full momentum transfer (FMT) fission.

The existing method to select FMT fission, based on reconstruction of the fission source velocity [16,21], was refined in this work by the introducing a geometrical factor ($\sin\theta_{c.m.}$) multiplying $(v_{||} - v_{CN})$, allowing more accurate gating of FMT events as a function of angle.

The measured mass-angle distributions for FMT fission events showed no evidence for a mass-angle correlation. The fission mass-splits appeared to be centered on symmetry at all angles. The absence of any evidence for fast quasifission is consistent with previous measurements over a more limited angular range for reactions of these projectiles on lighter actinide target nuclei. To our knowledge, the lightest projectile element in actinide reactions to show convincing evidence of a component with a mass-angle correlation, indicative of fast quasifission, is Mg, in the ${}^{24}\text{Mg} + {}^{238}\text{U}$ [2] and ${}^{26}\text{Mg} + {}^{248}\text{Cm}$ [42] reactions.

The FMT fission angular distributions did show evidence for quasifission, and without an observed mass-angle correlation, this must be associated with slow quasifission, where the system remains together for a least one rotation after contact. To reach this conclusion, it was important that reliable FMT fission differential cross-sections were obtained as a function of angle, even for the ${}^9\text{Be}$ induced reactions (which can have a large fraction of transfer-fission). A new method was developed for quantitatively subtracting transfer fission components underlying the FMT fission events. From these, angular distributions were obtained, and fitted within the TSM

formalism to obtain total FMT fission cross sections and angular anisotropies.

The extracted FMT fission cross sections were fitted with the coupled-channels model to estimate the angular momentum distributions for FMT fission. These were then used in the TSM model to calculate the angular anisotropies expected if the measured fission events resulted exclusively from fusion-fission.

The experimental anisotropies were larger than those expected for fusion-fission, which is generally taken as evidence for a component of quasifission. The deviation of the experimental anisotropies from expectations for fusion-fission showed a consistent increase with projectile mass (or charge). It also increased as the beam energy was reduced below that of the average capture barrier. This is consistent with previous measurements with lighter actinide target nuclei for ^{16}O , ^{12}C , and other projectiles [2,16,17].

Of particular note are the ^9Be FMT fission anisotropies, which showed two significant features.

- (i) At above-barrier energies, the experimental anisotropies are close to the TSM predictions for fusion-fission. This result supports the use of the TSM to calculate anisotropies for fusion-fission even for such heavy compound nuclei. Thus, the higher anisotropies measured above-barrier for $^{16}\text{O} + ^{244}\text{Pu}$ and $^{12}\text{C} + ^{248}\text{Cm}$ cannot be attributed to failure of the TSM, but must be associated with the presence of a “nonequilibrium” fission component, i.e., slow quasifission.
- (ii) At subbarrier energies, however, the anisotropies for the ^9Be reactions were significantly higher than the TSM predictions. Measurements for ^9Be at fixed beam energy resulted in different values of E/V_B for targets from ^{249}Cf to ^{238}U . The increase was largest at the lowest E/V_B , decreasing as the ratio of beam energy to capture barrier energy increased. This behavior is similar to that seen for ^{12}C and ^{16}O as a function of energy on the same targets. However, the increases above the predictions for fusion-fission seen for ^9Be are much smaller than for ^{12}C and ^{16}O . This can be interpreted as a smaller component of slow quasifission in collisions of ^9Be with the tips of the prolate deformed actinide target nuclei. This result is consistent with the smooth variation in the probability of slow quasifission parameterized as a function of projectile atomic number in Ref. [2].

A detailed study of the fission mass distributions in the reactions $^9\text{Be} + ^{249}\text{Cf}$, $^{12}\text{C} + ^{248}\text{Cm}$ and $^{16}\text{O} + ^{244}\text{Pu}$ forming $^{258,260}\text{No}$ was carried out, to investigate whether evidence for the presence of quasifission is also seen in the mass distributions.

The reason to expect a different mass distribution for slow quasifission, even if the mass degree of freedom is fully equilibrated, arises from the difference in the mean excitation energy from which fission occurs in quasifission compared to fusion-fission. Fusion-fission from the compact compound nucleus results in multichance fission, where fission occurs

not only from the initial excitation energy, but also following evaporation of one, two and more neutrons [30,34]. In contrast, at the low excitation energies in this study, even the slowest quasifission should occur faster than the lifetime for neutron evaporation, thus the excitation energy will be higher than the average for fusion-fission.

What are the effects of a higher excitation energy on mass distributions? Shell effects are responsible for the mass-asymmetric fission of actinide nuclei [43]. With increasing excitation energy, the effects of shells are quite quickly attenuated, reducing the mass-asymmetric structure in the mass distribution. Thus, the presence of slow quasifission should act to reduce the mass-asymmetric structure, even if the quasifission was slow enough that the mass evolution away from the entrance-channel asymmetry had completely equilibrated.

The measured mass distributions were inconsistent with a Gaussian distribution peaked at mass-symmetry, instead showing strong evidence for mass-asymmetric structure, consistent with the Standard II fission mode that is dominant in most actinide nuclei. Taking the ratio of the measured spectrum to that of the best-fitting single Gaussian function, the size of the deviation was quantified. At the same initial excitation energy, the mass-asymmetric structure was most significant for the $^9\text{Be} + ^{249}\text{Cf}$ reaction, less significant for $^{12}\text{C} + ^{248}\text{Cm}$ and least significant for $^{16}\text{O} + ^{244}\text{Pu}$. This is consistent with an increasing probability of quasifission with projectile charge (or mass). This correlates well with the increasing evidence for quasifission seen in the angular anisotropies, which is a completely independent observable.

V. CONCLUSIONS

By investigating mass, mass-angle and angular distributions of fission following capture for ^9Be , ^{12}C and ^{16}O reactions forming $^{258,260}\text{No}$, consistent evidence in both the angular and mass distributions was found for a contribution from quasifission. Since no correlation of mass with angle was seen, within the classical model of mass evolution in quasifission [5,44], any quasifission must be slower than the rotation time of the system.

The above-barrier angular distributions for $^9\text{Be} + ^{249}\text{Cf}$ (and also $^9\text{Be} + ^{248}\text{Cm}$, ^{244}Pu , ^{238}U) were close to transition-state model calculations for fusion-fission. This supports the use of the saddle-point TSM as a baseline, even in this highly fissile mass region, to investigate the presence of quasifission.

The angular distributions and mass distributions were consistent with previous conclusions that the slow quasifission probability increases as the projectile charge Z increases, and as the beam energy falls below the capture barrier. Even for the lowest Z projectile (^9Be), evidence for quasifission subbarrier was seen in the fission angular anisotropies. This suggests the probability of quasifission varies smoothly with changes in the colliding system, with no abrupt threshold.

The change in mass distributions between ^9Be and ^{16}O was small, suggesting that the quasifission component is essentially fully equilibrated in mass-split, but occurs before neutron evaporation, being faster than fusion-fission.

This is the first set of cross-bombardment measurements on actinide target nuclei showing evidence of slow quasifission simultaneously in both angular and mass distributions.

Comparison of these new experimental results with calculations of angular and mass distributions not only for fusion-fission, but also for slow quasifission, using dynamical models, would be a valuable next step to understand the dynamics of quasifission. As a quantum many-body process, this is a challenging task: the current extensive data set may help to guide and test such developments.

ACKNOWLEDGMENTS

This work was supported by ARC Discovery Projects No. DP160101254, No. DP170102318, and No. DP170102423. Operation of the ANU Heavy Ion Accelerator Facility was supported by the Australian Federal Government NCRIS HIA project. The authors thank Mr. Thomas Tunngley (ANU, Canberra) for producing Fig. 1, and Dr. Vanessa Robins (ANU, Canberra) for providing the derivation of the 2D Gaussian integral. Ch. E. Düllmann acknowledges the financial support from DAAD during the early phase of the preparation of the actinide targets in a collaboration with ANU.

APPENDICES

1. Geometrical factor correcting v_{\parallel}

The equation used [16] to extract v_{\parallel} is

$$v_{\parallel} = \frac{u_1 w_2 + u_2 w_1}{u_1 + u_2}, \quad (\text{A1})$$

where u_i and w_i are the projections of the laboratory frame fission fragment velocities parallel and perpendicular to the

beam axis respectively. This equation assumes that fission is a pure two-body process. However, particles (principally neutrons) are evaporated from the system both before and after scission, perturbing the kinematics. The effect of such perturbation on the extracted values of v_{\parallel} is illustrated for two center of mass angles: $\theta_{c.m.}=90^\circ$ in Fig. 17(i) and $\theta_{c.m.}=30^\circ$ in Fig. 17(ii). Multiple sources of fragment emissions were similarly identified by Moretto *et al.* in the 1980s [45].

In the figure the center of mass frame fission velocities $VF1_{c.m.}$ and $VF2_{c.m.}$ are shown in black. For pure two-body kinematics with a center of mass velocity v_{CN} (in the beam direction), laboratory frame fission velocities $VF1_{lab.}$ and $VF2_{lab.}$ result, as shown by the red arrows. Application of equation 7 gives $v_{\parallel} = v_{CN}$ for both fission c.m. angles. This is represented in the sketched distributions of $\Delta V_{\parallel} = v_{\parallel} - v_{CN}$ below by the red peaks at $\Delta V_{\parallel}=0$.

Now consider the result of isotropic emission before fission of a monoenergetic particle from the fissioning system initially moving with v_{CN} . This will result in a distribution of fission source velocities comprising a spherical shell in velocity space of radius ΔV , centred at v_{CN} . This is represented in two dimensions in Fig. 17 by the circles of radius ΔV . In the laboratory frame the fission velocities are both equally perturbed, as indicated by the blue circles centered on the unperturbed (red) laboratory fission velocities.

To evaluate the consequences, first let us consider fission occurring at $\theta_{c.m.}=90^\circ$, as shown in Fig. 17(i). The blue arrows represent the fission fragment laboratory velocity

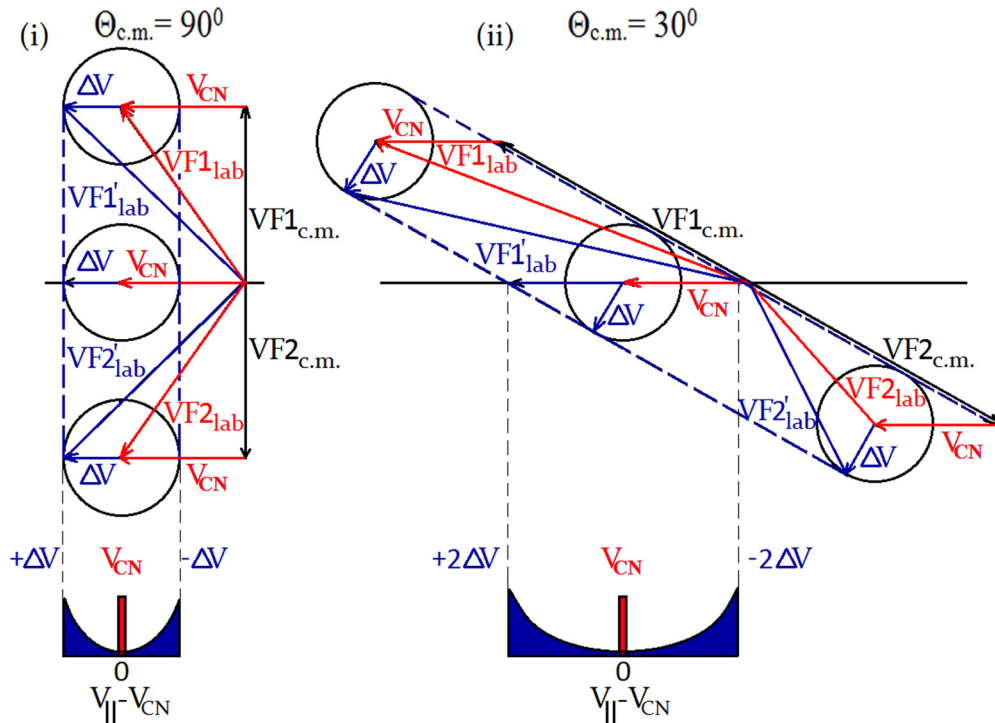


FIG. 17. Illustration of the effect of deviations of fission from a strictly two-body process, as a result of emission of light particles. The left-hand side of the figure (i) shows that at $\theta_{c.m.}=90^\circ$, for an isotropic velocity perturbation of magnitude Δv (see text), the extrema of the distribution (sketched below) of the fission fragment source velocities expressed as $\Delta V_{\parallel}=(v_{\parallel}-v_{CN})$, as extracted using Eq. (A1), are $\pm\Delta V$, exactly as expected. In contrast, the right-hand side of the figure (ii) shows that at $\theta_{c.m.}=30^\circ$, the extrema of ΔV_{\parallel} are at $\pm 2\Delta V$. It can be shown that the deduced values of $\Delta V_{\parallel}=(v_{\parallel}-v_{CN})$ should be multiplied by $\sin\theta_{c.m.}$ to give distributions of ΔV_{\parallel} that are independent of $\theta_{c.m.}$.

vectors corresponding to the largest positive perturbation of v_{\parallel} from v_{CN} . Application of equation 7 gives the deviation of ΔV_{\parallel} of magnitude ΔV , correctly returning the initial deviation. The resulting distribution of ΔV_{\parallel} is sketched below as the blue shaded region peaking at $\pm\Delta V$, with a minimum at $\Delta V_{\parallel} = 0$.

Fission at $\theta_{\text{c.m.}} = 30^\circ$, as illustrated in Fig. 17(ii) gives a quite different result. The maximum projection of the fission source velocity onto the beam axis v_{\parallel} results from ΔV components both in the beam direction *and* perpendicular to the beam direction, as indicated by the diagonal ΔV vectors. Application of equation 7 results in the extrema of ΔV_{\parallel} being $\pm 2\Delta V$.

It can be shown that for a perturbation of magnitude ΔV , the extrema in $\Delta V_{\parallel} = v_{\parallel} - v_{\text{CN}}$ occur at $\pm\Delta V/\sin\theta_{\text{c.m.}}$. This geometrical factor causes the experimental distributions of $v_{\parallel} - v_{\text{CN}}$ versus v_{\perp} to become increasingly elliptical as the angle of the fission event moves away from $\theta_{\text{c.m.}} = 90^\circ$, as shown in the upper panels of Fig. 3.

This geometrical effect can be simply corrected by multiplying the deduced quantity $(v_{\parallel} - v_{\text{CN}})$ by $\sin\theta_{\text{c.m.}}$, resulting in angle-independent distributions of $(v_{\parallel} - v_{\text{CN}})\sin\theta_{\text{c.m.}}$, as shown in the lower panels of Fig. 3.

2. Determination of the background from the azimuthal transfer-fission in the FMT region

A fraction of transfer-fission events will lie in the same region in $([v_{\parallel} - v_{\text{CN}}], v_{\perp})$ as the FMT events, i.e., around $(0, 0)$. These result because the transfer process can impart a velocity to the targetlike nucleus that has only a small component in the $([v_{\parallel} - v_{\text{CN}}], v_{\perp})$ plane, but a large component orthogonal to the plane. Physically this corresponds to the plane of the transfer process being close to the fission plane, and the scattering angle being close to $\theta_{\text{c.m.}} = 90^\circ$.

The distribution of transfer fission events in v_{\perp} can be derived by explicitly considering the third velocity component of the fissioning nucleus (v_{azimuth}), which is orthogonal to v_{\parallel} and v_{\perp} . This velocity component is normal to the beam and the plane of the fission event. The situation is shown in Fig. 18(a). Assuming that the azimuthal angles ϕ between the transfer and fission planes are populated isotropically, for any cut on $v_{\parallel} - v_{\text{CN}}$ in the region of FMT fission events, the transfer events will uniformly populate a set of circles for every transfer channel, each with their characteristic radius ΔV .

For a single transfer channel, with a single value of ΔV , projecting the circle onto the experimentally accessible variable v_{\perp} gives the intensity distribution $Y(v_{\perp})$ shown in Fig. 18(b), which has the functional form

$$Y(v_{\perp}) = \frac{K}{\Delta v \sqrt{1 - \left(\frac{v_{\perp}}{\Delta v}\right)^2}}. \quad (\text{A2})$$

Applying a gate [as sketched in Fig. 5(b)] to the experimental v_{\perp} spectrum of known width around the extrema [shaded blue in Fig. 18(b)] can provide from the centroid the mean value of ΔV , and from the yield the intensity normalization constant K . The latter is derived making use of the integral of

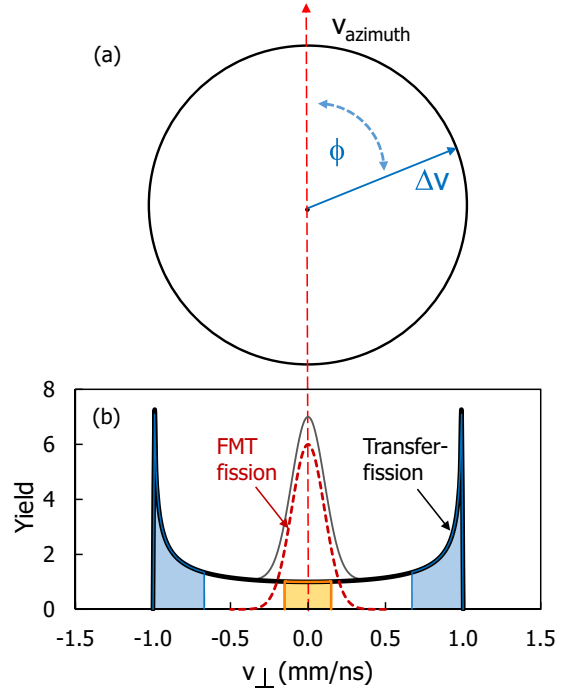


FIG. 18. (a) shows the idealized distribution of transfer fission events from a single transfer channel in the plane perpendicular to the beam, for a cut on ΔV_{\parallel} around zero. (b) Assuming an isotropic population of azimuthal angles ϕ between the fission plane and the transfer plane, the distribution projected onto v_{\perp} is presented by the thick curve. A FMT fission component is shown by the red dashed Gaussian. The azimuthal transfer fission underlying the FMT peak (shaded orange) can be determined through evaluation of the transfer fission events at the extreme values of v_{\perp} , shaded in blue (see text).

$Y(v_{\perp})$ between the limits v_1 and v_2 :

$$\int_{v_1}^{v_2} Y(v_{\perp}) dv_{\perp} = \left[K \sin^{-1} \left(\frac{v_{\perp}}{\Delta v} \right) \right]_{v_1}^{v_2}. \quad (\text{A3})$$

This equation can then give the azimuthal transfer fission yield in the range of v_{\perp} used to select the peak of the FMT fission events, as sketched in Fig. 5(c) and indicated by the orange shaded region in Fig. 18(b). As an example, 54% of the yield is found in the range $0.67\Delta V < |v_{\perp}| \leq \Delta V$. The range $0 < |v_{\perp}| \leq 0.15\Delta V$ [shaded orange in Fig. 18(b)] corresponds to the FMT fission cut, in which only 9.6% of the total transfer-fission yield is found. Thus, the cleanly measured transfer fission yield in the blue gated region should be scaled by $9.6/54$, corresponding to a reduction by a factor 5.6, to give the yield of azimuthal transfer fission inside the FMT fission gate, as indicated by the orange shaded region.

For each value of $v_{\parallel} - v_{\text{CN}}$ in the experimental spectrum, this procedure was followed, giving the expected counts of transfer fission within the FMT gate as a function of $v_{\parallel} - v_{\text{CN}}$. This is how the spectra shown in Fig. 6 by the blue dash-dotted curves, labeled azimuthal transfer, have been determined.

- [1] D. J. Hinde, R. du Rietz, M. Dasgupta, R. G. Thomas, and L. R. Gasques, *Phys. Rev. Lett.* **101**, 092701 (2008).
- [2] D. J. Hinde, D. Y. Jeung, E. Prasad, A. Wakhle, M. Dasgupta, M. Evers, D. H. Luong, R. du Rietz, C. Simenel, E. C. Simpson, and E. Williams, *Phys. Rev. C* **97**, 024616 (2018).
- [3] R. du Rietz, D. J. Hinde, M. Dasgupta, R. G. Thomas, L. R. Gasques, M. Evers, N. Lobanov, and A. Wakhle, *Phys. Rev. Lett.* **106**, 052701 (2011).
- [4] J. Khuyagbaatar *et al.*, *Phys. Rev. C* **97**, 064618 (2018).
- [5] W. Q. Shen, J. Albinski, A. Gobbi, S. Gralla, K. D. Hildenbrand, N. Herrmann, J. Kuzminski, W. F. J. Müller, H. Stelzer, J. Tke, B. B. Back, S. Bjørnholm, and S. P. Sorensen, *Phys. Rev. C* **36**, 115 (1987).
- [6] A. Wakhle, C. Simenel, D. J. Hinde, M. Dasgupta, M. Evers, D. H. Luong, R. du Rietz, and E. Williams, *Phys. Rev. Lett.* **113**, 182502 (2014).
- [7] E. Prasad, A. Wakhle, D. J. Hinde, E. Williams, M. Dasgupta, M. Evers, D. H. Luong, G. Mohanto, C. Simenel, and K. Vo-Phuoc, *Phys. Rev. C* **93**, 024607 (2016).
- [8] J. Khuyagbaatar, D. J. Hinde, I. P. Carter, M. Dasgupta, Ch. E. Düllmann, M. Evers, D. H. Luong, R. du Rietz, A. Wakhle, E. Williams, and A. Yakushev, *Phys. Rev. C* **91**, 054608 (2015).
- [9] Y. Aritomo and M. Ohta, *Nucl. Phys. A* **753**, 152 (2005).
- [10] B. B. Back, R. R. Betts, J. E. Gindler, B. D. Wilkins, S. Saini, M. B. Tsang, C. K. Gelbke, W. G. Lynch, M. A. McMahan, and P. A. Baisden, *Phys. Rev. C* **32**, 195 (1985).
- [11] I. Halpern and V. M. Strutinsky, Proc. Int. Conf. Peaceful Uses of Atomic Energy, Geneva, **15**, 408 (1958).
- [12] A. C. Berriman, D. J. Hinde, M. Dasgupta, C. R. Morton, R. D. Butt, and J. O. Newton, *Nature* **413**, 144 (2001).
- [13] J. Khuyagbaatar *et al.*, *Eur. Phys. J. A* **46**, 59 (2010).
- [14] J. Khuyagbaatar *et al.*, *Phys. Rev. C* **86**, 064602 (2012).
- [15] D. J. Hinde, M. Dasgupta, J. R. Leigh, J. P. Lestone, J. C. Mein, C. R. Morton, J. O. Newton, and H. Timmers, *Phys. Rev. Lett.* **74**, 1295 (1995).
- [16] D. J. Hinde, M. Dasgupta, J. R. Leigh, J. C. Mein, C. R. Morton, J. O. Newton, and H. Timmers, *Phys. Rev. C* **53**, 1290 (1996).
- [17] J. C. Mein, D. J. Hinde, M. Dasgupta, J. R. Leigh, J. O. Newton, and H. Timmers, *Phys. Rev. C* **55**, R995(R) (1997).
- [18] K. Nishio, H. Ikezoe, S. Hofmann, D. Ackermann, Y. Aritomo, V. F. Comas, C. E. Düllmann, S. Heinz, J. A. Heredia, F. P. Heßberger, K. Hirose, J. Khuyagbaatar, B. Kindler, I. Kojouharov, B. Lommel, M. Makii, R. Mann, S. Mitsuoka, I. Nishinaka, T. Ohtsuki *et al.*, *Nucl. Data Sheets* **119**, 299 (2014).
- [19] W. Parker and R. Falk, *Nucl. Instr. and Meth.* **16**, 355 (1962).
- [20] A. Vascon, S. Santi, A. A. Isse, T. Reich, J. Drebert, H. Christ, Ch. E. Düllmann, and K. Eberhardt, *Nucl. Instr. Meth. A* **696**, 180 (2012).
- [21] R. du Rietz, E. Williams, D. J. Hinde, M. Dasgupta, M. Evers, C. J. Lin, D. H. Luong, C. Simenel, and A. Wakhle, *Phys. Rev. C* **88**, 054618 (2013).
- [22] E. Prasad, D. J. Hinde, E. Williams, M. Dasgupta, I. P. Carter, K. J. Cook, D. Y. Jeung, D. H. Luong, C. S. Palshetkar, D. C. Rafferty, K. Ramachandran, C. Simenel, and A. Wakhle, *Phys. Rev. C* **96**, 034608 (2017).
- [23] P. J. A. Buttle and L. J. B. Goldfarb, *Nucl. Phys. A* **176** (2), 299 (1971).
- [24] D. M. Brink, *Phys. Lett. B* **40**, 37 (1972).
- [25] R. A. Broglia and A. Winther, *Heavy Ion Physics*, Parts I and II (Addison-Wesley Publishing Company, Redwood City, CA, 1991) Eq. (6), p. 116.
- [26] J. Wilczynski and H. W. Wilschut, *Phys. Rev. C* **39**, 2475 (1989).
- [27] K. Hagino, N. Rowley, and A. T. Kruppa, *Comput. Phys. Commun.* **123**, 143 (1999).
- [28] A. J. Sierk, *Phys. Rev. C* **33**, 2039 (1986).
- [29] J. P. Lestone, A. A. Sonzogni, M. P. Kelly, and R. Vandenbosch, *J. Phys. G: Nucl. Part. Phys.* **23**, 1349 (1997).
- [30] D. Ward, R. J. Charity, D. J. Hinde, J. R. Leigh, and J. O. Newton, *Nucl. Phys. A* **403**, 189 (1983).
- [31] D. J. Hinde, D. Hilscher, H. Rossner, B. Gebauer, M. Lehmann, and M. Wilpert, *Phys. Rev. C* **45**, 1229 (1992).
- [32] D. Peterson, W. Loveland, O. Batenkov, M. Majorov, A. Veshikov, K. Aleklett, and C. Rouki, *Phys. Rev. C* **79**, 044607 (2009).
- [33] J. P. Lestone, *Nucl. Data Sheets* **112**, 3120 (2011).
- [34] R. Leguillon, K. Nishio, K. Hirose, H. Makii, I. Nishinaka, R. Orlandi, K. Tsukada, J. Small-combe, S. Chiba, Y. Aritomo, T. Ohtsuki, R. Tatsuzawa, N. Takaki, N. Tamura, S. Goto, I. Tsekhanovich, C. M. Petrache, and A. N. Andreyev, *Phys. Lett. B* **761**, 125 (2016).
- [35] K.-H. Schmidt, B. Jurado, C. Amouroux, and C. Schmitt, *Nucl. Data Sheets* **131**, 107 (2016).
- [36] E. K. Hulet, J. F. Wild, R. J. Dougan, R. W. Lougheed, J. H. Landrum, A. D. Dougan, P. A. Baisden, C. M. Henderson, R. J. Dupzyk, R. L. Hahn, M. Schädel, K. Sümmerer, and G. R. Bethune, *Phys. Rev. C* **40**, 770 (1989).
- [37] D. C. Hoffman, D. M. Lee, K. E. Gregorich, M. J. Nurmia, R. B. Chadwick, K. B. Chen, K. R. Czerwinski, C. M. Gannett, H. L. Hall, R. A. Henderson, B. Kadkhodayan, S. A. Kreek, and J. D. Leyba, *Phys. Rev. C* **41**, 631 (1990).
- [38] J. F. Wild, E. K. Hulet, R. W. Lougheed, K. J. Moody, B. B. Bandong, R. J. Dougan, and A. Veeck, *J. Alloys Comp.* **213/214**, 86 (1994).
- [39] U. Brosa, S. Grossmann, and A. Müller, *Phys. Rep.* **197**, 167 (1990).
- [40] M. D. Usang, F. A. Ivanyuk, C. Ishizuka, and S. Chiba, *Sci. Rep.* **9**, 1525 (2019).
- [41] G. Scamps and C. Simenel, *Nature* **564**, 382 (2018).
- [42] I. M. Itkis, E. M. Kozulin, M. G. Itkis, G. N. Knyazheva, A. A. Bogachev, E. V. Chernysheva, L. Krupa, Y. T. Oganessian, V. I. Zagrebaev, A. Y. Rusanov, F. Goennenwein, O. Dorvaux, L. Stuttgé, F. Hanappe, E. Vardaci, and E. de Goés Brennand, *Phys. Rev. C* **83**, 064613 (2011).
- [43] G. Scamps and C. Simenel, *Phys. Rev. C* **100**, 041602(R) (2019).
- [44] J. Töke, R. Bock, G. X. Dai, A. Gobbi, S. Gralla, K. D. Hildenbrand, J. Kuzminski, W. F. J. Müller, A. Olmi, H. Stelzer, B. B. Back, and S. Bjørnholm, *Nucl. Phys. A* **440**, 327 (1985).
- [45] L. G. Moretto and G. J. Wozniak, *Prog. Part. Nucl. Phys.* **21**, 401 (1988).